Structure of the solar atmosphere: a radio perspective

C. E. Alissandrakis

Abstract Solar radio emission has been providing information about the sun for over half a century. In order to fully exploit this information, one needs to have a broader view of the solar atmosphere, which cannot be provided by radio observations alone. The scope of this chapter is to present this background information, which is necessary to understand the physical processes that determine the solar radio emission.

1 Introduction

By definition, the atmosphere of a star is the region from which photons can escape and reach the observer. Photons are not our only source of information for the sun; important information can also be obtained from particles originating on the sun and reaching the vicinity of the earth, both in the form of the quasi-steady flow of the solar wind and during energetic events. The magnetic field carried by the solar wind plasma is also an important carrier of information. Still, the bulk of what we know about the sun comes from photons, thus in this chapter we will restrict ourselves to the the results obtained from the analysis of the solar electromagnetic emission, in an attempt to compile a concise, but still comprehensive picture of the structure of the solar atmosphere; we will also try to give a historical perspective, as far as possible. More details can be found in a number of monographs on the sun (Kuiper [96], Zirin [199, 198], Foukal [66], Durrant [51], Priest [152], Stix [176], Aschwanden [13]) and on solar radio astronomy (Kundu [101], Zheleznykov [197], Krüger [99]). There also reviews on the quiet sun radio emission that the reader might be interested in (Alissandrakis [4], Gary [67], Alissandrakis and Einaudi [6],

C. E. Alissandrakis
Department of Physics, University of Ioannina, GR-45110 Ioannina Greece, and LESIA, Observatoire de Paris-Meudon e-mail: calissan@cc.uoi.gr

Lantos [116], Shibasaki [168], Keller and Krucker [89] and Shibasaki, Alissandrakis and Pohjolainen [169]).

As a rule, the term *structure* refers to the description of physical parameters as a function of position (in three dimensions) and time. As far as the time scale is concerned, solar phenomena are divided in three groups: the quiet sun, the slowly varying component and the sporadic component. This grouping also reflects the energy associated with the phenomena, with the sporadic emission being the most energetic. Here we will not discuss sporadic phenomena, but we will only consider the quiet sun and the slowly varying component that form the background for the more energetic phenomena.

It is important to stress that, as the the solar emission extends over a wide spectral range, from γ-rays to radio waves, no single spectral window can provide complete information on solar phenomena. Yet, for reasons that have to do with the instrumentation and the effects of the earth's atmosphere, astronomical observations refer to particular spectral windows. Each spectral window offers unique information, radio being no exception. Addressing an audience of solar radio astronomers, we will try to emphasize what this spectral range has offered to our understanding of the sun and to integrate radio data with data from other spectral ranges.

Although this chapter is about the sun's atmosphere, we will start with a brief section on its interior, which plays the role of the source for all atmospheric phenomena. We will continue with a discussion of the radial structure of the solar atmosphere and then with its horizontal structure. We will then pass to active regions and we will finish with a discussion of the heating problem.

2 From the core to the solar atmosphere

Until a few decades ago, we had no direct information about the interior of the sun; what we knew was based on the theory of stellar structure, which produced the so called *standard model* of the solar interior. The most important conclusion, apart from the fact that conditions in the solar core are appropriate for the fusion of hydrogen to helium through the proton-proton cycle, is that the interior of the sun is radiative up to $\sim 0.71\mathrm{R}_\odot$, where convection starts and operates up to the subphotospheric layers. The convection zone has huge implications on the solar dynamo [145, 36], producing the magnetic field observed in the atmospheric layers and governing their structure.

The detection of neutrinos produced by nuclear fusion reactions in the solar core opened up a new area of research [42]. However, it turned out that neutrino astronomy gave us more information about the properties of neutrinos [1], rather than the solar interior. Real observational information about the interior of the sun came with helioseismology (see review by Christensen-Dalsgaard [40]).

When velocity oscillations were discovered by Leighton, Noyes and Simon [122] and by Evans and Michard [55], they were considered to be a local phenomenon. It was thanks to the works of Deubner [45] and Hill [34], that their true character, as global acoustic (p-mode) oscillations for which the sun acts like a cavity, was revealed. The oscillations are also observed in intensity, easily detectable as small fluctuating elements, in certain spectral ranges such as the UV continuum around 1700 Å, as shown in Fig. 1.

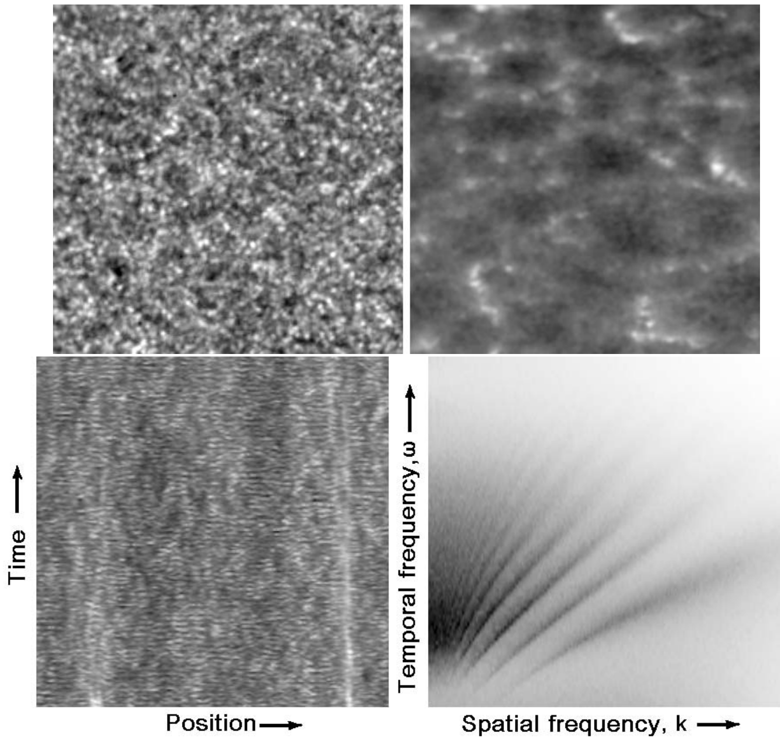

Fig. 1 A quiet region observed with TRACE in the 1700 Å band (top left), processed to show only oscillating elements. A time average of the same region over 4 hours in the top right panel shows the enhanced emission associated with the network (see Section 5.2). A position-time cut of the intensity (bottom left) shows the wavy nature of the spatio-temporal variations, verified by the ω-k diagram of the bottom right panel, which clearly shows the ridges associated with the acoustic waves

Helioseismological spectral data are as rich in spectral lines as the optical solar spectrum or even richer, and their inversion allows us to measure quantities such as the speed of sound and the speed of rotation in the solar interior. The most impressive results are the excellent agreement with the standard model (Fig. 2, left) and the rigid rotation of the solar interior (Fig. 2, right) below the convection zone. However, if the revised, significantly lower, abundances of C, N, and O, are used [14], there is an important discrepancy between helioseismology and solar interior models which has not found a satisfactory solution yet.

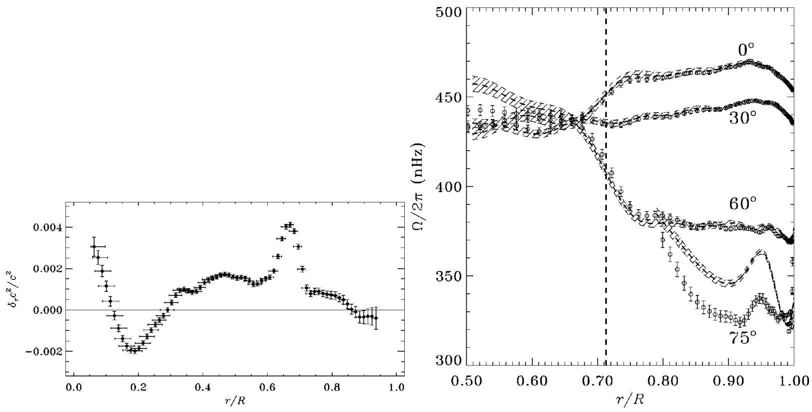

Fig. 2 Helioseismology results: Deviation of the measured speed of sound from that predicted by the standard model of the solar interior (left, from [21]) and angular velocity of solar rotation as a function of latitude and distance from the center of the sun (right, from Christensen-Dalsgaard [40]). The vertical dashed line marks the bottom of the convection zone.

As can be seen in Fig. 2, p modes cannot probe the deep solar interior; g modes, for which gravity (buoyancy) is the restoring force, are much better in this respect [12]. However, gravity waves cannot propagate in a convectively unstable medium, such as the convection zone; they are evanescent there and are expected to come out in the photosphere with a much reduced, undetectable yet, amplitude.

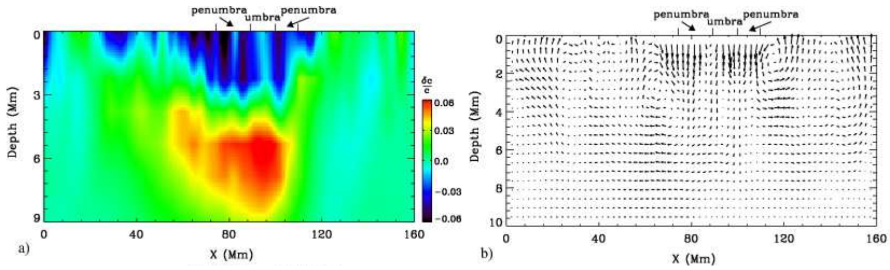

Fig. 3 Structure of the sun below a sunspot: Perturbation of the speed of sound (left) and flow velocity (right) from time-distance helioseismology. Note that the vertical scale is much more expanded than the horizontal. From Zhao, Kosovichev, and Sekii [193]

With the advent of time-distance seismology, we have also been able to map the horizontal structure of the solar interior, in the sub-photospheric layers [77, 93]. Impressive results have been obtained, such as those shown in Fig.3: two layers appear in the structure of a spot below the photosphere, one with negative sound-speed perturbation (*i.e.* temperature lower than the average) and downflows in the top 4 to 5 Mm and one with a positive perturbation in deeper layers. Similar results were reported in [78] and more are expected as the method is refined and the quality of observations improves.

3 Atmospheric structure

3.1 Elementary physics of the solar atmosphere

Part of energy radiated by the sun reaches the earth and it can be measured. From the value of the *solar constant* (the energy per unit area per unit time at 1 AU), together with the solar radius and the sun-earth distance, the effective temperature of the visible layer of the solar atmosphere (the *photosphere*) can be computed. Its value of 5800 K gives us a measure of the photospheric temperature, and this is very important information.

Let us note further that in visible light the sun appears as a disk with a sharp limb. From this elementary remark we can infer that the photospheric density decreases very fast with height, i.e. that the density scale height is much smaller than the solar radius. Indeed, under the (crude) isothermal approximation, let us start from the equation of hydrostatic equilibrium,

$$\frac{dp}{dz} = -g\rho \tag{1}$$

where p is the pressure, g the gravity (assumed constant) and ρ the density. We can further express the pressure in terms of the density, using the equation of state,

$$p = NkT = \frac{\rho}{\mu_{mol} m_H} kT \tag{2}$$

where N is the number density of particles, μ_{mol} is the mean molecular weight (=1 for an atmosphere of neutral Hydrogen, 0.5 for fully ionized Hydrogen, 0.61 for 10% Helium), m_H the hydrogen mass, k the Boltzmann constant and T the temperature. Integrating (1) we obtain:

$$\rho = \rho_o e^{-z/H} \tag{3}$$

where ρ_o is the density at $z = 0$ and

$$H = \frac{kT}{g\mu_{mol} m_H} \tag{4}$$

is the isothermal scale height. Expressions similar to (3) hold for the pressure and for the number density. For the effective temperature of the photosphere, the scale height is a mere 175 km, *i.e.* just 0.0025 $R_\odot$, which tells us that the photosphere is very thin and, at the same time, explains why the optical limb is so sharp.

Another well known fact is that, during total eclipses of the sun and at the time that the moon has covered completely the photosphere, a bright red-colored crescent appears, the *chromosphere*; its extent is certainly greater than that of the photosphere and this, following the argument about the scale height, implies that it has a higher temperature. The fact that it is much fainter than the photosphere, indicates that it has also a much lower density. Finally, much more extended, faint and diffuse than the chromosphere is the *corona*, which appears when the chromosphere has been covered by the moon. Again this implies very high temperature, much higher than that of the chromosphere, and very low density. Last but not least, the huge temperature difference between the chromosphere and the corona requires a *chromosphere-corona Transition Region* (TR) to bridge the two.

Thus, using simple physical arguments, we have discovered the principal layers of the solar atmosphere and we have come across a basic problem of solar physics: that of the heating of the chromosphere and the corona, which we will discuss further in section 7

3.2 Extracting the information

In order to go beyond the elementary arguments of the previous section, we have to know how the physical conditions influence the production and transport of photons. The electromagnetic radiation that comes to us is rich in information about the physical conditions in the region of its formation, such as the electron temperature, the electron density and pressure, the magnetic field, the velocity of flow, the abundance of elements etc. It is the astrophysicist's task to extract this information and the main tool for this is the theory of radiative transfer [134, 160]. Without going into the details, let us remind the reader that the specific intensity, I_ν, observed at the frequency, ν, that reaches the observer from a stellar atmosphere is given by the formal solution of the transfer equation for a plane-parallel, semi-infinite atmosphere:

$$I_\nu(\tau_\nu = 0, \mu) = \int_0^\infty S_\nu e^{-t_\nu/\mu}\, dt_\nu/\mu \tag{5}$$

Here the integration is carried along the vertical direction, z, which forms an angle θ with the path of the radiation (i.e. with the line of sight, in the absence of refraction), hence the presence of $\mu = \cos\theta$ in Equation (5); the position along the vertical is expressed in terms of the optical depth, τ_ν, which is related to the geometrical height, z, and the opacity of the material through:

$$d\tau_\nu = -k_\nu \rho dz \tag{6}$$

where ρ is the density of the material and k_ν is the absorption coefficient, which depends on the prevailing emission/absorption processes. The minus sign is because the optical depth is measured from the observer to the star, while z is measured in the opposite direction. Furthermore, S_ν in Equation (5) is the *source function*, which is the ratio of the coefficients of emission, j_ν, and absorption, k_ν,

$$S_\nu = \frac{j_\nu}{k_\nu} \tag{7}$$

and expresses the emissivity of the material; it is equal to the Plank function, $B_\nu(T)$, under conditions of Local Thermodynamic Equilibrium (LTE).

From the very form of Equation (5), we can see that the specific intensity carries information about all atmospheric layers and that the contribution of each layer is weighted by the local value of the source function and reduced by the absorption of overlying layers. It is easy to prove that, in first order approximation, the observed specific intensity corresponds to the value of the source function at $\tau_\nu = \mu$ (Eddington-Barbier relation); thus at the center of the disk we see at $\tau = 1$.

Fig. 4 Solar images on October 7, 2009 in the blue part of the spectrum (left) in the red (middle) from the Mauna Loa Solar Observatory (MLSO) and at $\lambda = 5.2$ cm from the Siberian Solar Radio Telescope (SSRT)

In practice, we can probe the atmosphere by two means. One is by varying μ, which is can be done by measuring the variation of the specific intensity from the center of the solar disk where $\mu = 1$ to the limb, where $\mu = 0$. It is also easy to show that, if the temperature decreases with height, the intensity at the limb is lower than at the disk center (limb darkening); in the opposite case the limb is brighter. Fig. 4 shows three full disk solar images. Two of them, in the optical range, show limb darkening (more in the blue than in the red part of the spectrum), which proves that the temperature is decreasing with height in the region of formation of the radiation (photosphere); the third, in the microwave range, shows signs of limb brightening, which indicates that the temperature is rising above the photosphere, where the radiation is formed.

The second method for probing the atmosphere is by varying the frequency of observation, which changes the opacity; for obvious reasons, this variation is weak in the continuum and very strong in spectral lines. As Fig. 5 shows, this method allows us to probe a height range of ~ 600 km, where the temperature ranges from ~ 4500 K to ~ 6700 K. This requires a fairly broad spectral range, from sub-mm λ to the far ultraviolet, as shown in the figure.

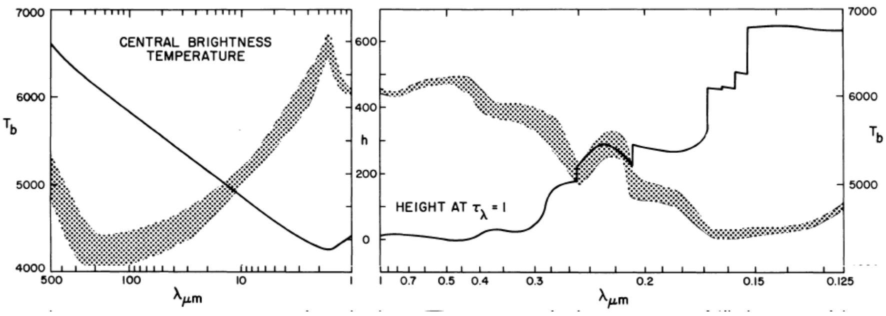

Fig. 5 Observed continuum brightness temperature at the center of the solar disk as a function of wavelength (shaded band) and the approximate height of formation of the radiation (from [186])

It follows from the above discussion that, in principle, one could invert Equation (5) and recover the information on the physical conditions. This is the basis for the computation of *empirical* atmospheric models (see Chapter 6.10 in [198]). Things are not simple though, because of the complex dependence of the absorption coefficient on the physical conditions and due to departures from LTE. The situation is better in the radio range, thanks to the Rayleigh-Jeans approximation to the Planck function and the fact that electrons, which are responsible for thermal emission, are always in LTE. Under these circumstances, the solution of the transfer equation takes a much simpler form:

$$T_b = \int_0^\infty T_e e^{-t_\nu/\mu} \, dt_\nu/\mu \tag{8}$$

which links the electron temperature, T_e, with the observed brightness temperature, T_b (see Equation (2) in introduction by Klein for a definition of T_b).

We will finish the section by considering the emission of a homogeneous slab of material (cloud), overlying a background of specific intensity $I_{\nu o}$:

$$I_\nu = I_{\nu o} e^{-\tau_\nu} + S_\nu (1 - e^{-\tau_\nu}) \tag{9}$$

or, for the radio range,

$$T_b = T_{bo} e^{-\tau_\nu} + T_e (1 - e^{-\tau_\nu}) \tag{10}$$

An important consequence of these relations is that, if the slab is optically thick, a measurement of the brightness temperature gives us directly the value of the electron temperature ($T_b \simeq T_e$, for $\tau_\nu >> 1$). If, on the contrary, the slab is optically thin ($\tau_\nu << 1$) and there is no background emission, its brightness temperature is lower than its electron temperature:

$$T_b = \tau T_e \tag{11}$$

4 Radial structure of the solar atmosphere

In our discussion in the previous section we implicitly assumed that solar parameters vary only in the radial direction. However, anyone who has seen solar images will agree that the Sun is extremely rich in horizontal structures and that inhomogeneities become more prominent as we move from the photosphere to the chromosphere and the corona. Moreover, as the spatial resolution of our instruments increases, we become more and more aware of the importance of horizontal structures.

Under these circumstances, it is rather surprising that one-dimensional models which, in addition to treating the physical parameters as a function of height only, also assume hydrostatic equilibrium, have any resemblance to the observations at all. The physical reason behind the success of such models is gravity, which produces a strong radial stratification in the solar atmosphere; as a consequence, the radial density gradient is much larger than the horizontal, at least in the lower atmospheric layers.

In this section we will present and discuss various one-dimensional empirical models of the solar atmosphere, from the photosphere to the corona.

4.1 Empirical models for the low atmosphere

There is a long tradition of 1-D empirical solar models. The Bilderberg Continuum Atmosphere (BCA [75]), which superseded the Utrecht Reference Photosphere (URP [82]), was the first to take into account mm-wave observations together with EUV data; a comparison between BCA-predicted brightness temperatures and observations in the range of 0.0086 – 15.8 mm was presented in Fig. 7 of [143]. The Harvard Smithsonian Reference Atmosphere (HSRA; [76]) followed, and the brightness computations and comparison with data were extended to 10 cm (Fig. 3 in [76]).

These models did not extend beyond the chromosphere; they all stopped around $T_e \simeq 10^4$ K, which is too low for model computations in the cm radio wavelength range and beyond. The Vernazza, Avrett and Loeser (VAL) models that followed [185, 186, 187] extended the temperature range up to 3×10^4 K, into the lower part of the transition region. The subsequent Fontenla, Avrett and Loeser (FAL) models [56, 57, 58] went up to 10^5 K, while one model of the same authors [59] went up to 1.2×10^6 K, in the upper TR. These models also developed further the multi-component approach, first introduced in [187], to represent different quiet and active regions on the Sun. Note that multi-component models are not really 3-D, since radiative transfer in the horizontal direction is not taken into account.

In the more recent works [60, 61, 62], the emphasis shifted again to the lower atmospheric layers (up to 10^4 K). Still, Avrett and Loeser [18] produced a model of the average quiet Sun chromosphere and TR up to 1.6×10^6 by extending model C (average quiet Sun) of [60]. The authors computed, among other things, the spectrum in the range of 0.04 –40 mm. Their results are shown in Fig. 6, together with

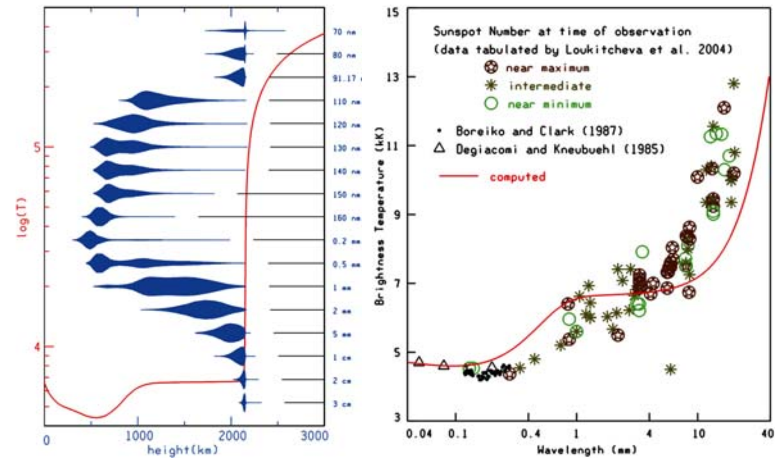

Fig. 6 The variation of temperature with height, according to the model of Avrett and Loeser [18], together with contribution functions at several wavelengths, including microwave (left panel); the corresponding spectrum is shown in the right panel.

the temperature vs. height variation of their model and the contribution functions at several wavelengths, including some in the short microwave range. Note that the extent of the photosphere is only a few hundred km, in agreement with the arguments presented in Section 3.1. Note also that the microwave spectrum reproduces, as expected, the shape of the $T_e(z)$ curve. According to this figure, most of the emission at 3 cm and shorter wavelengths originates below the TR, with a small contribution from the latter and practically no contribution from the corona.

In order to compute brightness spectra at longer wavelengths, one has to add a coronal contribution. Zirin, Baumert and Hurford [200] found that their measurements, which extended up to 21 cm, could simply be reproduced by a two-component model: an optically thick chromosphere and an isothermal corona. We know, however, that there is a TR between these two (see further discussion in Section 4.3.2). In a recent work, Selhorst, Silva and Costa [167] used a hybrid model (combination of models for the photosphere, chromosphere, and corona) to reproduce the observed features in Nobeyama Radioheliograph (NoRH) images at 17 GHz. To obtain acceptable brightness temperature values and the observed solar radius, they had to include absorbing chromospheric structures, such as spicules (see section 5.3) into the model, as has been done in the past (*e.g.* [115]), in order to explain why the observed center-to-limb variation shows less brightening than the homogeneous models predict, or even shows darkening. Their computed spectrum is shown in Fig. 7, together with a model by Bastian Dulk and Leblanc [20] that covers approximately the same frequency range.

The results presented in Fig. 6 and 7 show that a model can be found that fits most microwave data, although there is a large scatter in the mm to sub-mm range due to inherent difficulties in the measurements and possible solar cycle effects. The

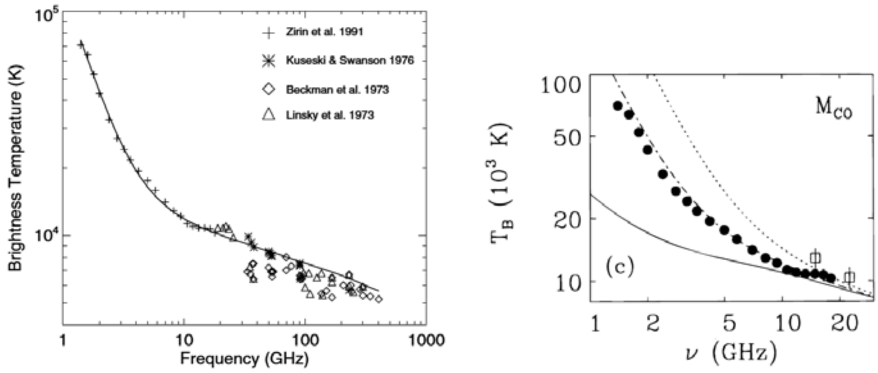

Fig. 7 *Left*: Observed brightness temperatures of the solar disk center (symbols) and the hybrid model fit (solid line) of Selhorst, Silva and Costa [167], presented over a wide frequency range. *Right*: Spectra computed by Bastian Dulk and Leblanc [20]; solid line: on the basis of a model by Avrett [17]; dot-dashed line: with the addition of a minimum corona inferred by Zirin, Baumert and Hurford [200]; dotted line: with the addition of three-times the minimum corona. Filled circles are the measurements of Zirin, Baumert and Hurford [200], squares are VLA measurements by the authors.

main problem with these models is that the radio data are better fitted with models that represent the *cell interior*, rather than with average models, which predict too much radio flux.

4.2 Emission measure and differential emission measure

All computations of the quiet sun radio emission presented above start from standard atmospheric models. In a different approach, several authors have tried to use direct information from the EUV part of the spectrum to compute the radio brightness, which is reasonable since the radiation in both wavelength ranges is formed in the same atmospheric layers. In one approach the emission measure, EM, which is a measure of the electron density, N_e, along the line of sight, is used:

$$EM = \int_0^L N_e^2 d\ell \tag{12}$$

This quantity appears in the expression for the integrated intensity of EUV lines:

$$I = \frac{1}{4\pi}\int_0^L G(T_e,N_e)\,N_e^2\,d\ell \simeq \frac{1}{4\pi} < G(T_e,N_e) > EM, \tag{13}$$

where $G(T_e,N_e)$ is the contribution function for the line.

The emission measure also appears in the expression for the radio brightness temperature; for an isothermal layer and negligible refraction we get from Equation (6):

$$\tau = \xi \frac{1}{f^2 T_e^{3/2}} \int_0^L N_e^2 d\ell = \xi \frac{EM}{f^2 T_e^{3/2}} \quad (14)$$

where we used the standard expression for the absorption coefficient at the frequency f [101],

$$k_j(T_e, N_e) = \xi \frac{N_e^2}{n_j f^2 T_e^{3/2}} A_j(B, \theta) \quad (15)$$

Here ξ is a slowly varying function of T_e and N_e ($\xi \sim 0.12$ in the chromosphere and $\sim$0.2 in the corona), n_j is the index of refraction (~ 1 at short wavelengths) and $A_j(B, \theta)$ is a function of the magnitude of the magnetic field B and its angle with the line of sight, θ [197]. Note that here k is used instead of $k\rho$ in Equation (6).

Furthermore, if the emitting layer is optically thin (cf Equation (10)),

$$T_b \simeq \tau T_e = \xi \frac{EM}{f^2 T_e^{1/2}}. \quad (16)$$

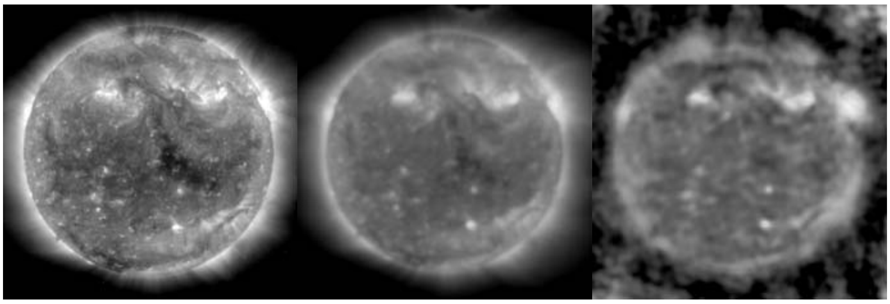

Fig. 8 EIT image at 195 Å (left), computed brightness (middle), and observed (VLA) brightness at 20 cm for November 11, 1997. Figure adapted from Zhang *et al.* [194]

It is a well known practice to use two EUV lines for an estimate of the plasma temperature and the emission measure. Zhang *et al.* [194] used three EIT images, at 171, 195 and 284 Å, to derive the emission measure in a two-temperature model. They used this information to compute the emission at 6 and 20 cm wavelengths, which they compared with their VLA observations. Fig. 8 shows their results at 20 cm. Although the model image looks very much like the observed, the computed brightness temperature was twice the observed at both wavelengths. They attributed the discrepancy to errors in the coronal abundances used to infer the radio flux from the EIT data. Their results also raise the question of accuracy in temperature and emission measure computations from broad-band EUV images.

The differential emission measure (DEM) is even better than the emission measure; it is defined as

$$\varphi(T_e) = N_e^2 \frac{d\ell}{dT_e} \quad (17)$$

and represents the distribution of electron density over a temperature range T_1 to T_2. Equations (13) and (14) are then replaced by

$$I = \frac{1}{4\pi}\int_{T_1}^{T_2} G(T_e, N_e)\varphi(T_e)dT_e \quad (18)$$

$$\tau = \frac{\xi}{f^2}\int_{T_1}^{T_2} T_e^{-3/2}\varphi(T_e)dT_e \quad (19)$$

and the isothermal assumption is dropped. Obviously, one needs many EUV lines, formed over the appropriate temperature range, in order to make good use of the DEM.

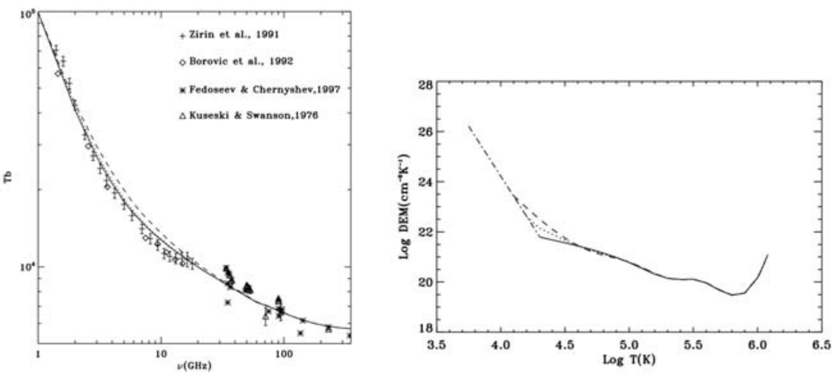

Fig. 9 Spectra computed by Landi and Chiuderi Drago [114] (left) and the corresponding differential emission measure (right).

Landi and Chiuderi Drago [113] used the DEM values derived from UV and EUV spectral line intensities observed by SUMER and CDS, and showed that a TR model *for the cell interior* – excluding any network contribution – could give an agreement with the observed radio brightness temperatures. In a subsequent work [114], the same authors showed that radio observations provide a much more reliable diagnostic tool for the determination of the DEM than UV and EUV lines at $T < 30\,000$ K, since the latter are optically thick. Moreover, they extended the DEM down to 5600 K using the radio spectrum from 1.5 to 345 GHz, and obtained very good agreement with the radio data (Fig. 9).

4.3 Coronal and Transition Region models

4.3.1 Models from optical and EUV Data

As mentioned already in Section 3.1, the extent of the corona indicates a large scale height and a high temperature. Emission lines in the optical spectrum (the emission line or *E-corona*), also provide evidence for a hot corona. These lines, originally attributed to an unknown element (coronium), turned out to be due to forbidden transitions of highly ionized species, such as Fe X (the red line at 6374 Å), Fe XIV (the green line at 5303 Å) and Ca XV (the yellow line at 5494 Å); they were identified thanks to the work of Grotrian [79] and of Edlén [52]. The issue of their formation temperature was not settled, until dielectronic recombination was taken into account (for a vivid account see Chapters 6.3 and 7.3 in Zirin's book [199]).

Due to the difficulties in the interpretation of the line emission, coronal models are based on the continuum white light corona, which is due to Thomson scattering of photospheric photons on the free electrons of the coronal plasma [184]. This emission is linearly polarized and constitutes the *K corona (kontinuierlich)*; there is also unpolarized emission (the *F corona*), which is due to Rayleigh scattering in dust and small particles that exist between the sun and the earth.

Assuming spherical symmetry, a number of models have been produced [2, 184, 136, 161] from K corona data. In spite of the fact that the corona is highly inhomogeneous, some of them, namely the Newkirk [136] and Saito [161] models are still in use; they are very useful in modeling the radio emission and in estimates of the height of radio sources (see chapter by Klein). The Newkirk model predicts a variation of the electron density, n, with the distance, r, from the center of the sun that has the form:

$$N_e = 4.2\,10^4\,10^{4.32R_\odot/r} = 4.2\,10^4\,e^{9.95R_\odot/r} \tag{20}$$

which is hydrostatic, since solution of the hydrostatic equilibrium equation (1), in spherical coordinates and taking into account the variation of gravity with height, takes the form:

$$N_e = N_{eo}e^{-\frac{R_\odot}{H_\odot}+\frac{R_\odot}{H_\odot}\frac{R_\odot}{r}} \tag{21}$$

where $H_\odot$ is the scale height at the base of the corona. A comparison of the Newkirk model with the hydrostatic gives (*cf.* chapter by Klein),

$$N_{eo} = 8.8\,10^8 \text{ cm}^{-3} \tag{22}$$

$$H_\odot = 0.1005R_\odot = 70\,000 \text{ km} \tag{23}$$

this value of the scale height corresponds to a coronal temperature of $T = 1.41\,10^{\,6}$ K.

The Saito model allows for density variations with latitude, φ:

$$N_e = \frac{3.09\cdot 10^8(1-0.95\sin\varphi)}{(r/R_\odot)^{16}} + \frac{1.58\cdot 10^8(1-0.5\sin\varphi)}{(r/R_\odot)^{6}} + \frac{0.0251\cdot 10^8(1-\sqrt{\sin\varphi})}{(r/R_\odot)^{2.5}} \tag{24}$$

The polar corona reflects coronal hole conditions, but coronal holes were not known at the time. The Saito model is close to hydrostatic; the best fit in the range of 1 to $2R_\odot$ is obtained for a scale height of $0.103R_\odot$ (coronal temperature $T_c = 1.44\cdot 10^6$ K). At $r = R_\odot$ the model gives lower densities than the Newkirk model: $4.7\,10^8$ cm^{-3} at the equator and $9.5\,10^7$ cm^{-3} at the poles.

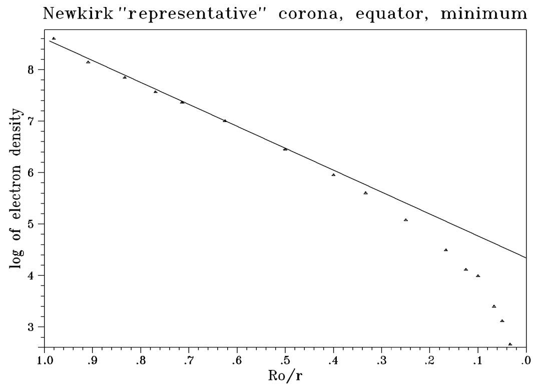

Fig. 10 Equatorial "representative" equatorial coronal density at minimum, after Table I of Newkirk [137], as a function of the inverse distance from the center of the sun, up to $30R_\odot$. The solid line represents the hydrostatic model.

Far from the photosphere, the hydrostatic model is not valid; indeed, Equation (21) predicts a finite density, $n_o \exp(R_\odot H_\odot)$, when r goes to infinity; moreover, the limiting value for the sun is five orders of magnitude above the density of the interplanetary medium. This means nothing other than that the corona cannot be in hydrostatic equilibrium and we know very well that it is not, as the supersonic, superalfvénic *solar wind* sets up, with the sonic point located near $\sim 3R_\odot$. The fall of the measured electron density below the values predicted by the hydrostatic model is clearly seen in plots of the electron density as a function of distance, such as that in Fig. 10 (see also Fig. 4 of Koutchmy [109], reproduced as Fig. 3 in the introductory chapter [Klein]). In one case, the departure of the density from the hydrostatic model was used to estimate the velocity of solar wind flow [111], which was found consistent with the theory.

Between the chromosphere and the corona there is a thin (a few thousand km) *Transition Region* (TR), where the temperature rises fast from $\sim 10^4$ K to $\sim 10^6$ K. Many ions have ionization states in this temperature range and emit spectral lines in the extreme ultraviolet range (EUV) of the spectrum. Early space observations of these lines [50, 15] indicated that the temperature structure of the TR is such that the conductive flux, from the corona to the chromosphere, is constant; this can be explained in terms of the thinness of the TR, due to which very little energy is radiated and there is no convection in any case. Under the constant conductive flux assumption, the temperature gradient is given by:

$$\frac{dT}{dz} = \frac{F_c}{A} T^{-5/2} \tag{25}$$

where F_c is the conductive flux and A is a constant with the value of $1.1\,10^{-6}$ cgs units. Integration gives:

$$T(z) = \left[T_o^{7/2} + \frac{7}{2} \frac{F_c}{A} (z - z_o) \right]^{2/7} \tag{26}$$

where T_o is the temperature at the reference height, z_o, which could be at any point within the TR.

Solving the hydrostatic equilibrium equation we get for the electron density:

$$N_e(T) = N_{eo} \frac{T_o}{T} \exp[-8.9\,10^{-11} (T^{5/2} - T_o^{5/2})/F_c] \tag{27}$$

As mentioned in section 4.1, some recent empirical models, such as that of Avrett and Loeser [18] shown in Fig. 6, include the TR. The model goes from the photosphere up to a temperature of $1.59\,10^6$ K, reached at a height of 68 000 km. It is an equilibrium model, taking into account the contribution of the dynamic pressure of turbulent motions to the total pressure. The conductive flux in the transition region ranges from $\sim 10^5$ at $2\,10^5$ K to $\sim 3\,10^5$ at $1.59\,10^6$ K with a representative value of $\sim 2.4\,10^5$.

4.3.2 Implications for the radio range

We can compute the optical depth of the TR in the radio range by first expressing Eq. (6) in terms of the temperature gradient [8]; we then get, using (25) and (15):

$$d\tau = -k \frac{dz}{dT} dT = -\Gamma \frac{dT}{T} \tag{28}$$

where $\Gamma = \xi A p^2 / f^2 F_c$, $p = N_e T$ is proportional to the pressure and refraction has been ignored. Since the TR is very thin, the pressure can be assumed constant and, ignoring also the small variation of ξ with temperature, the optical depth of a TR layer extending from T_1 to T_2 is given by integrating (28):

$$\tau_{TR} = \Gamma \ln \frac{T_2}{T_1} \tag{29}$$

Subsequent integration of the transfer equation gives the brightness temperature of the layer:

$$T_{b,TR} = \frac{\Gamma}{\Gamma+1}(T_2 - T_1\, e^{-\tau_{TR}}) = \frac{\Gamma}{\Gamma+1} T_2 \left[1 - \left(\frac{T_1}{T_2}\right)^{\Gamma+1}\right] \tag{30}$$

Substitution of numerical values shows that, in the microwave range, both $\Gamma << 1$ and $\tau_{TR} << 1$; thus we obtain from (30):

$$T_{b,TR} \simeq \Gamma (T_2 - T_1) \tag{31}$$

A similar computation can be done for an isothermal, hydrostatic corona. If the variation of the scale height with z is ignored, which is not a bad assumption for the microwave range where the coronal contribution comes from the lower layers, we get for the coronal τ, and T_b, after [8]:

$$\tau_c = 0.5\, k_c\, H \tag{32}$$

$$T_{b,c} = \tau_c\, T_c \tag{33}$$

Putting everything together, if we have a corona on the top of a transition region and a region with brightness temperature T_{bo} at the bottom, the observed brightness is:

$$T_b = T_{bo}\, \exp(-\tau_{TR} - \tau_c) + T_{b,TR}\, \exp(-\tau_c) + T_{b,c} \tag{34}$$

and, in the optically thin approximation:

$$T_b = T_{bo} + \Gamma (T_c - T_1) + \tau_c\, T_c \tag{35}$$

Note that, the second term in the rhs of Eq. (35), which represents the TR contribution, has the same form of frequency dependence ($\Gamma \propto f^{-2}$) as the third term, which represents the coronal contribution ($\tau_c \propto f^{-2}$). It is therefore not surprising that Zirin, Baumert and Hurford [200] could not distinguish between the transition region and the corona in their spectral measurements.

As we move from the cm to the meter range, the optical depth of the chromosphere-corona transition region (TR) and the corona increase, due to the growth of the absorption coefficient which is proportional to the square of the wavelength. At the same time, as the observing wavelength increases, the frequency approaches the plasma frequency, the index of refraction (see chapter Alissandrakis-2 for expressions) departs from unity and the rays eventually suffer total reflection (Fig. 11, left panel). As a result of refraction and reflection, the lower part of the corona is inaccessible. Moreover, the observed position of a localized source will be displaced towards the disk center, an effect which is stronger near the limb; a source may even appear in two places, if the optical depth along the path of the refracted ray is small. In any case, both the radiative transfer and the ray tracing equations should be solved for model computations.

Refraction effects are not important, unless the optical depth between the observer and the point of total reflection is small. This is illustrated in the right panel of Fig. 11, where the height of reflection, the optical depth up to reflection and the resulting brightness temperature are plotted as a function of frequency for the cen-

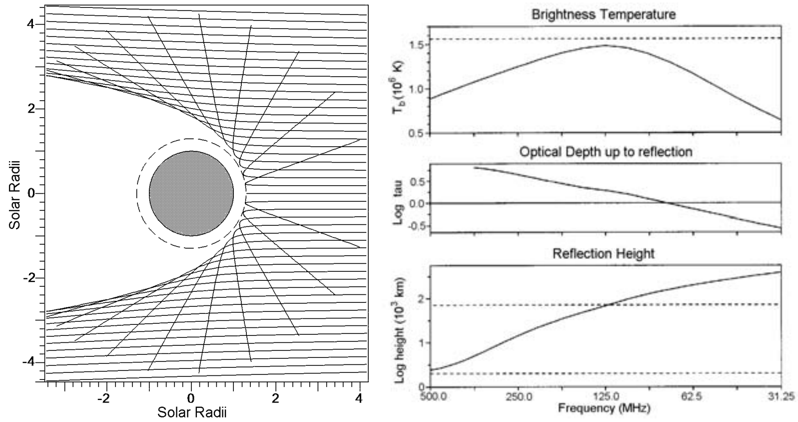

Fig. 11 Left: Ray paths at metric wavelengths, showing the effects of refraction and total reflection. Right: The height of reflection, the optical depth up to the reflection point and the brightness temperature as a function of frequency for the center of the solar disk. The ray tracing computations were performed for a Saito equatorial density model, with a coronal temperature of 1.52 10^6 K and a constant conductive flux TR with $F_c = 10^5$ erg cm^{-2} s^{-1} (from [4]).

ter of the solar disk. For frequencies higher than $\sim$125 MHz the reflection point is inside the TR (between the dashed lines at the bottom of the figure). However, radiation from the reflection point does not reach the observer because is is absorbed by the overlaying layers which are optically thick; thus the brightness temperature increases with decreasing frequency, as the effective depth of formation moves through the TR towards the corona. At longer wavelengths the rays are reflected before they accumulate sufficient optical depth and the brightness temperature decreases, remaining below the coronal electron temperature (dashed line, top panel of the figure).

The above predictions are verified by observations at long (metric) wavelengths, where there is a marked departure of the brightness temperature below the coronal electron temperature, with the brightness temperature showing a maximum of $\leq$ 10^6 K near 2-3 m (see Table 1 and Fig. 4 of Lantos [116]). In addition to refraction, scattering by random density fluctuations also plays a role [16, 83, 179, 180, 19, 181]. Scattering smooths sources of small angular size and increases the apparent size of the radio Sun; it also displaces sources in a direction opposite to that of refraction.

5 Horizontal structure

5.1 Theoretical issues

The importance of horizontal structure was pointed out in section 4. A basic question that we will address here is what determines the horizontal structure. In order to answer this question we will resort to plasma physics (see also Chapter 2 in [152] and Chapter 6 in [13]). We will start with the MHD equation of momentum transport:

$$\rho\left(\frac{\partial V}{\partial t}+V\cdot\nabla V\right)=\rho g-\nabla P+\frac{J\times B}{c} \tag{36}$$

where V is the plasma flow velocity, B the magnetic field, J the electric current density, P the pressure and g the gravity. The magnetic field acts upon the plasma through the *Lorentz force*, $J\times B/c$, which is perpendicular to the field. Using Ampère's law,

$$\nabla\times B=\frac{4\pi}{c}J \tag{37}$$

we can eliminate the current in the Lorentz force to get:

$$\frac{J\times B}{c}=-\nabla\frac{B^2}{8\pi}+\frac{B\cdot\nabla B}{4\pi} \tag{38}$$

which decomposes the Lorentz force to a *magnetic pressure* term:

$$P_m=\frac{B^2}{8\pi} \tag{39}$$

and a *magnetic tension* term which depends on the curvature of the magnetic field lines; indeed, the second term in the right hand side of Equation (38) can be written as:

$$\frac{B\cdot\nabla B}{4\pi}=\frac{B^2}{4\pi}\frac{\hat{n}}{R_c}+\nabla_\parallel\frac{B^2}{8\pi} \tag{40}$$

where $\nabla_\parallel$ is the component of the gradient parallel to the field, $\hat{n}$ is the unit vector perpendicular to the field, R_c is the curvature of magnetic field lines:

$$\frac{\hat{n}}{R_c}=\hat{b}\cdot\nabla\hat{b} \tag{41}$$

where $\hat{b}$ is the unit vector along the field. Going back to Equation (38), the Lorentz force can be written as:

$$\frac{J\times B}{c}=\nabla_\perp P_m+\frac{B^2}{4\pi}\frac{\hat{n}}{R_c} \tag{42}$$

the first term in the rhs being the magnetic pressure and the second the magnetic tension.

Since the Lorentz force acts perpendicular to the field, parallel to the field we can write from Equation (36):

$$\rho\left(\frac{\partial V_{\parallel}}{\partial t}+V_{\parallel}\cdot\nabla V_{\parallel}\right)=\rho g_{\parallel}-\nabla_{\parallel}P \tag{43}$$

Which is Bernouli's equation of flow in a flux tube. Moreover, if the plasma motion is slow, i.e.,

$$V \ll \sqrt{\frac{P}{\rho}} = v_s \quad \text{(sound speed)} \tag{44}$$

$$V \ll \frac{B}{\sqrt{4\pi\rho}} = v_A \ \text{(Alfvén speed)} \tag{45}$$

$$V \ll \sqrt{Lg} \sim v_g \quad \text{(free fall speed)} \tag{46}$$

the velocity terms in the momentum transfer equation can be ignored, and we get the hydrostatic equilibrium equation:

$$\nabla_{\parallel}P=\rho g_{\parallel} \tag{47}$$

which has the solution:

$$P=P_0 e^{-\int_{z_0}^{z}\frac{dz}{H(T)}} \tag{48}$$

where $H(T)=(kT)/(g\mu_{mol}m_H)$ is the scale height (*cf* section 3.1).

The conclusion from the above analysis is that, under the conditions specified by Equations (44) to (46), *each magnetic flux tube can have its own atmosphere*, as far as the pressure distribution is concerned. Moreover, since the heat conduction coefficient is much higher along the magnetic field then in the perpendicular direction, each flux tube can have its own temperature distribution.

Let us now consider the equation for the time variation of the magnetic field. Starting from Ohm's law:

$$E+\frac{V\times B}{c}=\eta J \tag{49}$$

where E is the electric field, J is the electric current density and η is the resistivity; substituting in Faraday's law,

$$\nabla\times E=-\frac{1}{c}\frac{\partial B}{\partial t} \tag{50}$$

we obtain the *induction equation*:

$$\frac{\partial B}{\partial t}=\frac{\eta c^2}{4\pi}\nabla^2 B+\nabla\times(V\times B) \tag{51}$$

In the case of

$$\frac{4\pi VL}{\eta c^2}\equiv R_m \ll 1, \tag{52}$$

where R_m is the magnetic Reynolds number, the second term in the right hand side of Equation (51) can be ignored; in this case the time evolution of the field is described by a diffusion equation:

$$\frac{\partial B}{\partial t} = \frac{\eta c^2}{4\pi} \nabla^2 B \tag{53}$$

and magnetic energy eventually goes to thermal energy, through Joule heating. In the opposite case the second term in the right hand side of Equation (51) dominates and the field is *frozen-in*:

$$\frac{\partial B}{\partial t} = \nabla \times (V \times B) \tag{54}$$

Almost everywhere in the solar atmosphere the magnetic Reynolds number is much larger than unity. The behavior of the plasma and the magnetic field then depends upon their relative energy density:

- If the energy density (thermal plus kinetic) of the plasma is much smaller than that of the field or, equivalently, if the sum of the gas pressure and the dynamic pressure is much smaller than the magnetic pressure, then the magnetic field dominates and the plasma flows along the field lines. This is the case in the chromosphere, the corona and in sunspots.
- In the opposite case the plasma dominates and will drag and deform the field. This happens in the photosphere (outside sunspots) and in the solar wind

As we will see further on in this chapter, this simple argument can explain qualitatively almost everything that we see on the sun. Of course, today we have in our disposal both powerful computers and efficient codes for solving numerically the MHD equations and we have seen spectacular results of simulations that can hardly be distinguished from real observations (see reviews by Nordlund, Stein and Asplund [142], Moradi *et al.* [135], Rempel and Schlichenmaier [157], Solanki, Inhester and Schüssler [172], Carlsson [35], de Wijn *et al.* [47]). Still, it is very important to have a sound understanding of the physical principles which are often hidden behind the simulations.

5.2 Photospheric structure

From the above discussion we expect plasma motion to dominate in the photosphere and drag the magnetic field lines. Indeed, the most prominent photospheric structure is the granulation, with a spatial scale of $\sim 1.5''$, and a temporal scale of ~ 15 min, which is attributed to convection currents (see the classic work by Bray and Loughhead [31] for a historic account, and recent reviews by Nordlund, Stein and Asplund, [142] and Rieutord and Rincon [158]). As can be seen in Fig 12, which shows intensity and velocity images of the photosphere at the center of the solar disk, hot material in the bright granules ascends, while cooler material in the dark inter-granular lanes descends; the same effect produces the zigzag appearance of photospheric absorption lines (see, e.g., Fig. 6.20 in [198]). As a matter of fact, the convection zone ends below the photosphere, which is convectionally stable; thus, the granulation is an effect of *overshoot* of convection into the stable layers of the photosphere.

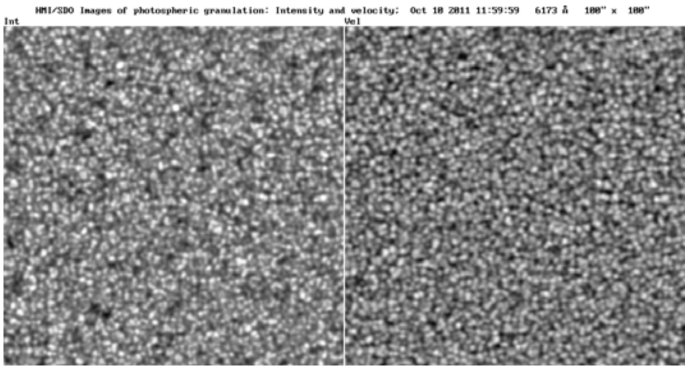

Fig. 12 Image of the photospheric granulation at the center of the disk (left), together with an image of the line of sight velocity (white towards the observer). The velocity has been averaged over 5 min to reduce the effect of oscillations. (Data from the *Helioseismic and Magnetic Imager* (HMI) aboard the *Solar Dynamics Observatory* (SDO))

The photospheric granulation is not the only convection system on the sun. A larger scale ($\sim$40$''$) and long lived ($\sim$20 h) convection system was detected in 1962 by Leighton, Noyes and Simon [122], as a horizontal flow pattern (Fig. 13). The pattern is better visible far from the center of the disk, where the horizontal flow translates to approaching and receding line of sight velocities. This has been called *supergranulation*. An intermediate scale convection system, the *mesogranulation* has been reported by November *et al.* [144], who used correlation tracking to measure horizontal flows. The three scales of convection would be associated with the ionization zones of HI, HeI and HeII. However, the existence of mesogranulation as distinct scale of convection has been contested; views have been expressed that it is an extension of granulation or even an artifact produced by the correlation tracking algorithm (see discussion in [142] and [158])

The development of time-distance helioseismology has given us some information on the depth of supergranulation, despite the inherent difficulties [93, 142]. According to Kosovichev and Duvall [94], supergranular flows appear down to 2-3 Mm below the surface; however the pattern disappears below $\sim$ 5 Mm, or is dominated by noise. Similar results were obtained by Jackiewicz, Gizon and Birch [85], see Fig. 14.

Under the influence of the plasma flows the magnetic field is deformed and dragged at the edge of supergranular boundaries. The compressed magnetic flux tubes appear as tiny bright features in intergranular lanes, best visible in very high resolution photographs taken in the G-band (Fig. 15, left). These were first detected by Dunn [48] and called *filigree*. Higher up, in the chromosphere, enhanced emis-

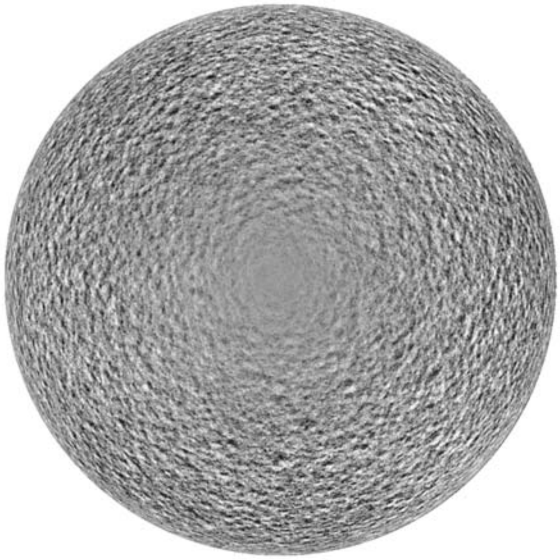

Fig. 13 Supergranulation cells, seen in a line of sight velocity image, corrected for solar rotation, from the *Michelson Doppler Imager* (MDI), aboard the *Solar and Heliospheric Observatory* (SOHO). This is the average of 45 images taken on January 13, 1996, over the time interval of 30 min.

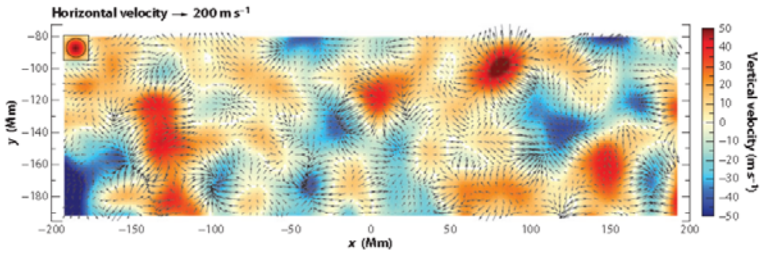

Fig. 14 Horizontal (arrows) and vertical (color) supergranulation flows, at a depth of 1 Mm, computed from the inversion of travel time measured over 3 days. From [85] and [77]

sion is observed above these regions (Fig. 15, right). The emission is more diffuse there, apparently due to the lateral expansion of the magnetic flux tubes. These regions of enhanced chromospheric emission constitute the well known *chromospheric network* which, as pointed out in [122], coincides with the borders of the supergranules. In spite of its name, the network has its roots in the photosphere, or even lower.

The convective flows not only drag the magnetic field; they also compress it to kilo Gauss strengths, as deduced first by Stenflo [174], from simultaneous measurements in lines with different Landé factors. Magnetic field of such strength cannot be confined by the plasma pressure alone, thus Parker [147] proposed that the field is further confined as a result of the adiabatic cooling of the descending plasma. Fig. 16 (left) shows a magnetogram of a quiet region near the center of the solar disk; the strong network field is accompanied with brightenings in the continuum around 1600 Å (center); the strongest magnetic features are associated with

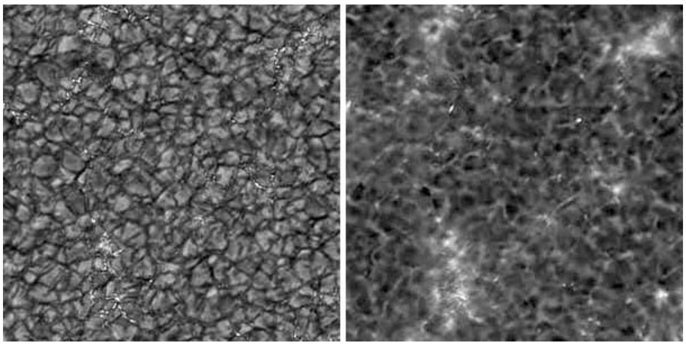

Fig. 15 Bright points near the center of the solar disk, as seen in the G-band (left) and in the Ca II H line (right). The field of view is ... Images taken with the *Dutch Open Telescope* (DOT) on ..., courtesy of R. Rutten.

persistent downflows (right). Note that the highest field value recorded is $\sim$700 G, apparently limited by the resolution of the instrument; the maximum downflow is $\sim$700 m/s, about a factor of 2 stronger than measured by [43]. Note also that the velocity image shows signs of granular convective motion, reminiscent of the "persistent" granulation [22], in spite of the 4 hour integration.

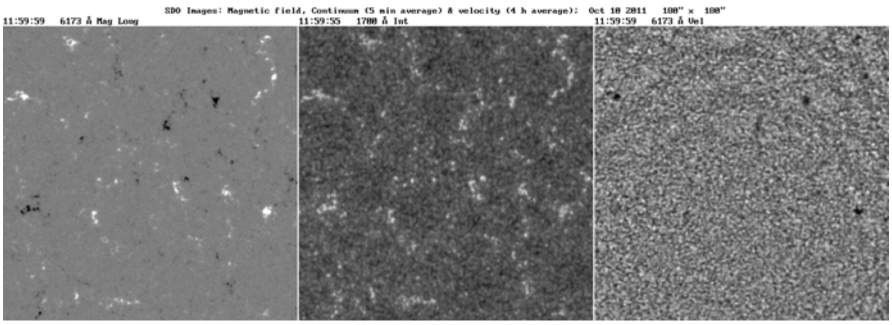

Fig. 16 Line of sight magnetic field from HMI/SDO (left), intensity in the 1700 Å band from AIA/SDO (middle) and line of sight velocity averaged over 4 hours from HMI/SDO (right); downflows are dark, upflows bright.

The fact that the vertical component of the magnetic field is strong at supergranular boundaries does not mean either that the internetwork region is devoid of field or that the field orientation is vertical. As demonstrated by the magnetogram of Fig. 16, small magnetic elements are practically everywhere [178]. As for the orientation of the magnetic field, recent results from the Solar Optical Telescope (SOT) aboard Hinode have shown that both vertical and horizontal fields exist and, moreover, more flux has been measured in horizontal fields than in vertical [123, 47].

In a recent work, Ishikawa and Tsuneta [87] proposed that internetwork magnetic fields are formed by the emergence of small scale flux tubes; the vertical magnetic field at their footpoints is intensified due to convective collapse and advected by the supergranular flow to form the network fields.

The network is well visible in the microwave radio range. Kundu *et al.* [106] were the first to obtain quiet Sun images at 6 cm wavelength with arc-second resolution with the Westerbork Synthesis Radio Telescope (WSRT). These images showed a clear association of the microwave emission with the chromospheric network, something that had already been suggested on the basis of interferometric (*e.g.*, [107, 103]) and one-dimensional (*e.g.*, [28, 72]) observations of the quit sun. This conclusion was subsequently verified with the Very Large Array (VLA) observations at 6 and 20 cm by Gary and Zirin [69], and Gary *etal* [70] at 3.6 cm. In the mid 90's the VLA was used for quiet Sun observations in the short cm-range (1.2, 2.0 and 3.6 cm) by a number of authors [20, 26, 98].

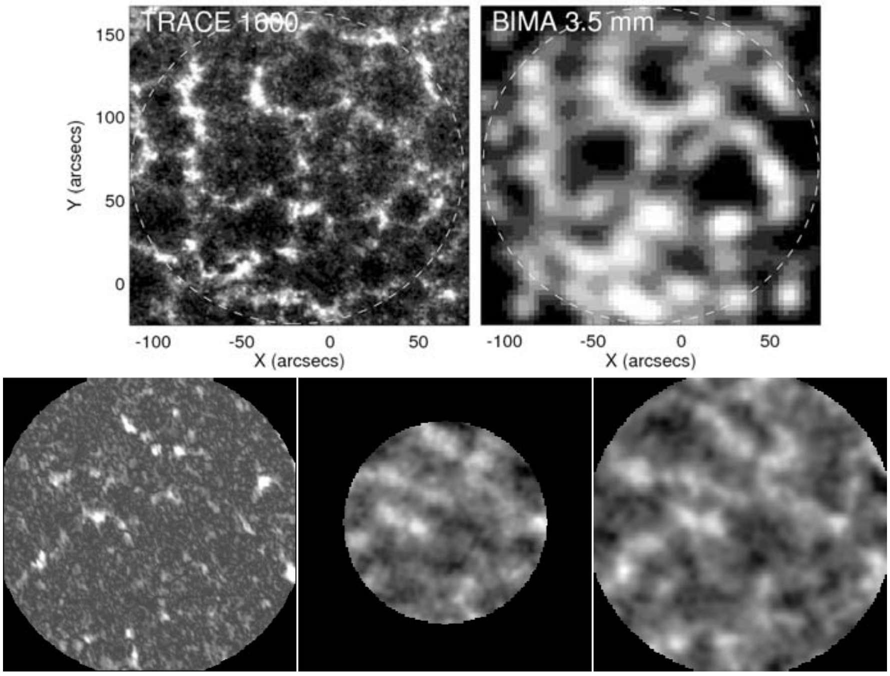

Fig. 17 High-resolution radio images of the quiet Sun in the mm-wave to short cm-wave range. (top): TRACE 1600 Å image together with the BIMA radio image at 3.5 mm (85 GHz) on May 18, 2004 (adapted from [126]). The field of view is 195″by 195″ and the spatial resolution is 12″; (bottom): Image of the absolute value of the photospheric magnetic field from KPNO (left), together with VLA radio images at 1.3 cm (23 GHz, middle) and at 2.0 cm (15 GHz, right) on September 23, 1992 (adapted from [20]). The field of view is 165 by 165″ in and the spatial resolution is 3.3″ and 5″ at 1.3 and 2 cm respectively.

In the mm-range, high-resolution images of the quiet Sun were first produced by White *etal* [190] and Loukitcheva *etal* [124]. They used the 10-element Berkeley-Illinois-Maryland Association Array (BIMA) in its most compact D-configuration, to obtain $\sim 10''$ resolution. BIMA images at 3.5 mm are shown in Fig. 17, together with VLA images at 1.3 and 2.0 cm, for comparison. In all cases the chromospheric network, delineated in the TRACE UV continuum images or the photospheric magnetograms, is the dominant structure in the radio images. Network structures appear broader in radio, but this effect almost disappears if one degrades the TRACE images to the resolution of the radio images.

In addition to the spatial coincidence of bright radio features with the chromospheric network, it is important to measure their intensity and size as a function of wavelength. We should note that interferometric/synthesis observations cannot measure the background level, which should be provided by other means. Thus, the most appropriate measure of the intensity fluctuations is their amplitude or, even better, their rms variation.

In all reported measurements, both the amplitude and the rms of spatial intensity variations increase with wavelength. According to Benz *etal* [26], the rms varies from 290 K at 1.3 cm to 930 K at 3.6 cm; these values are consistent with the ones given by Bastian *etal* [20] at 1.3 and 2 cm and they correspond to 2.8% and 5.8% variations respectively if reasonable values for the background are used. The actual increase with wavelength should be larger, due to the decrease of spatial resolution. At 6.1 cm, Gary and Zirin [69] give 8300 K and 21400 K above the background as the average value of individual source peak brightness in two regions, while Kundu *etal* [106] give absolute values of $\sim 2.5 \times 10^4$ and $\sim 1.5 \times 10^4$ K for typical network elements and cell interiors respectively at 6 cm. In the mm range, Loukitcheva *etal* [125] give 1100 K for the intensity variation.

These results have not been fully exploited in multicomponent models. Older computations by Ciuderi Drago *etal* [37], based on the VAL [187] model, do show an increase of brightness difference between network and cell interiors with wavelength, while the values reported in recent works are close to those computed by the above authors for the VAL model D (average network).

5.3 Structure of the chromosphere and the low corona

Above the photosphere, the energy density of the plasma drops dramatically due to the decrease of the density, whereas the magnetic energy density decreases at a slower rate. Eventually the magnetic field dominates over the plasma in the chromosphere and low corona and, as a result, a dramatic change in the morphology of fine structures is observed. Structures of convective origin, such as granules and magnetic bright points give way to elongated structures delineating the lines of force of the magnetic field.

This is illustrated in Fig. 18 where, in addition to the magnetogram of Fig. 16, images of the same region in the He II 304 Å and in the Fe XII 193 Å lines, formed

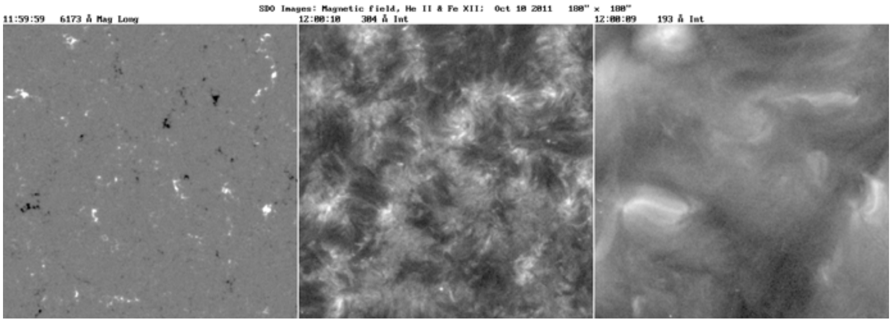

Fig. 18 Line of sight magnetic field from HMI/SDO (left), intensity in the HeII 304 Å band (middle) and in the FeXII 193 Å band (right) from AIA/SDO. Same region as in Fig. 16.

in the upper chromosphere and in the corona respectively, are shown. Ia addition to the extension of the network, the HeII image shows a multitude of small scale, low-lying loops, mostly in absorption (dark), joining regions of opposite magnetic polarity. Although the appearance of the coronal image is different, loops are still the basic structural element; here they all are in emission (bright), they are not as numerous as in HeII and there is a lot of diffuse emission in between. The latter is probably due to low intensity loops, too thin to be distinguished with the $\sim 1''$, resolving power of the instrument.

Note the absence of any trace of the network in the coronal image. This is well known from the Skylab era [155]: the network becomes diffuse in the upper transition region and disappears in the low corona, apparently as a result of fanning out of the magnetic field and field lines closing at low heights. A similar behavior is expected for the radio network, the main problem here being the variable spatial resolution. Bastian *etal.* [20] reported no detectable change in the size of network elements between 1.3 and 2 cm, after smoothing the 1.3 cm image to match the 2 cm resolution. There is a lack of imaging observations between 6 and 20 cm; in any case, the few published quiet sun images at 20 cm (*e.g.* [69], see also the 20 cm image in Fig. 8) do not show much of a network.

A more classical picture of the chromospheric fine structure is shown in Fig. 19, in the wing and at the center of the Hα line. Thin, elongated dark structures, known as *dark mottles*, emerge above the supergranular boundaries. They extend more or less vertically and are best visible in the blue wing of the line, revealing a predominantly upward motion. They are less prominent at the Hα line center where, in addition, fine *bright mottles* appear at their roots.

Seen at the limb, these structures appear as jet-like features (*spicules*, see [23, 24, 175, 149]), well visible in the wings of the Hα line. Spicules, with a typical lifetime of $\sim$10 min; they rise to height of up to $\sim$10 000 km with a velocity of $\sim$ 20 km s^{-1} and then either fall down or diffuse in the corona. A classic set of spicule images, scanning the Hα line with a 1/4 Å bandwidth filter, is shown in Fig. 20. These were the best images at the time they were taken (1970); today we can have

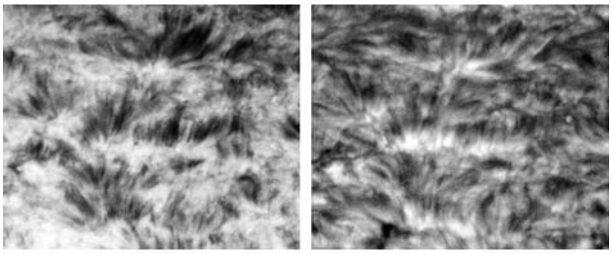

Fig. 19 A chromospheric region far from the center of the solar disk, in the blue wing of Hα (left) and in the center of the line (right). The field of view is 95$''$ by 80$''$. Photographs with the 40 cm *Tourelle* refractor at the Pic du Midi Observatory on September 27, 1979. Adapted from [5].

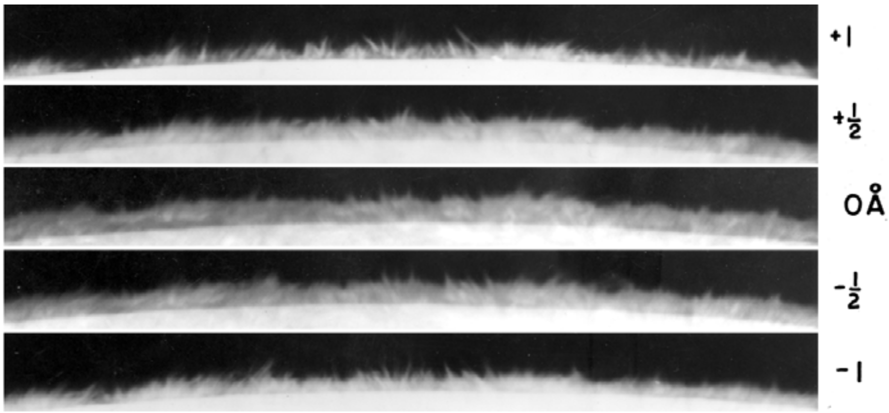

Fig. 20 Spicules at the limb, at the center and the wings of the Hα line. Observed by R. D. Dunn with the Vacuum Tower Telescope (now the Dunn Telescope) of the Sacramento Peak Observatory in 1970. Adapted from a figure published in [127]

much higher spatial resolution, as evidenced in Fig. 21, which shows structures as thin as a few tenths of an arc second. High resolution imaging from space, together with the improved resolution of ground-based observations, has led to a number of recent investigations both at the limb and on the disk. The new observations revealed the existence of a new type of spicules, *type II spicules* [46], which are both faster ($\sim$100 km s^{-1}) and short lived ($\sim$1 min, compared with ordinary spicules). However, the existence of type II spicules as a distinct class has been contested recently [195]. The other domain where new observations have had an enormous contribution is spicule oscillations (see Zaqarashvili and Erdélyi [192] for details).

Note that the appearance of chromospheric structure in different lines can be quite different, depending on the details of line formation. For example, limb structures seen in the He II 304 Å line are much much extended than Hα spicules and are known as *macrospicules*. An example is shown in Fig. 22, comparing spicules in

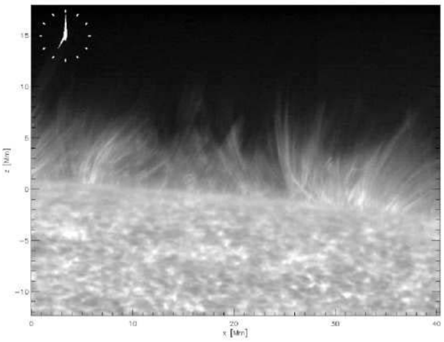

Fig. 21 Spicules at the limb observed in the CaII H line with the Solar Optical Telescope (SOT) aboard Hinode. From [86]

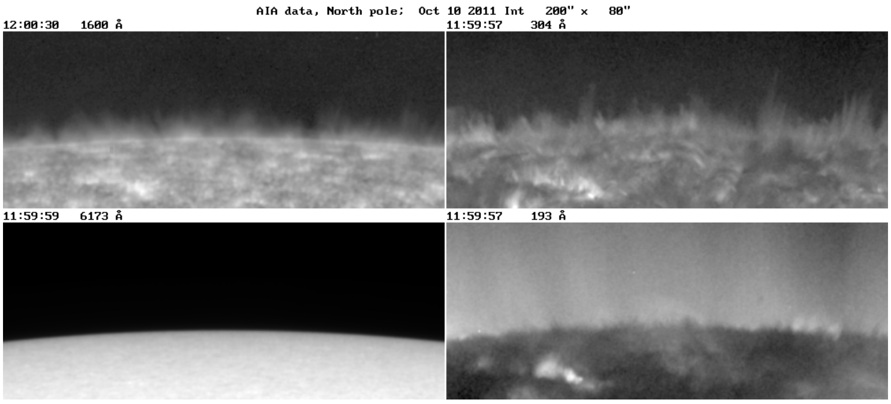

Fig. 22 SDO images of the limb near the north pole, in the 1600 Å band (top left), in the HeII 304 Å band (top right),in the continuum near 6173 Å (bottom left), and in the FeXII 193 Å band (bottom right).

the 1600 Å band of AIA/SDO (mostly emission from the CIV lines at 1548 Å) with macrospicules; a white light and a coronal image are included for reference.

The origin of spicules is still a subject of debate. As disk mottles are clearly associated with the network, a magnetic origin is very likely; what is not clear is whether they are a result of reconnection, as suggested by Pickelner a long time ago [150], the result of leakage of photospheric oscillations expelling plasma along the magnetic field lines, as suggested by De Pontieu, Erdélyi, and James [44], or the result of some other process. Numerical simulations may provide some clues.

In the microwave range, there has been only one report of structures beyond the limb [80], to the author's best knowledge. However, several authors have detected emission beyond the optical limb [106, 25, 166, 95], which makes the radio radius of the sun is larger than the optical. Chromospheric structures have also been invoked in the interpretation of the center to limb variation of the intensity. Limb brightening is expected in the microwave range, since the electron temperature increases with height in the region of formation of the radiation. The observations, however, show less brightening than predicted by homogeneous models, or even show darkening that cannot be attributed to the limited instrumental resolution. This is usually interpreted in terms of absorbing features, such as spicules (*e.g.* Lantos and Kundu [115], Selhorst, Silva, and Costa [167]). Note that, as cool spicules penetrate into the the hot corona (Fig. 22), they can act as absorbing agents; this is not the case with the chromosphere, where spicules are hotter than their surroundings [23, 24].

Another note-worthy observation is that polar regions are brighter than the low-latitude quiet Sun at short cm-waves to mm-waves. We will not discuss this in detail here, but we will refer the reader to the review by Shibasaki, Alissandrakis and Pohjolainen [169].

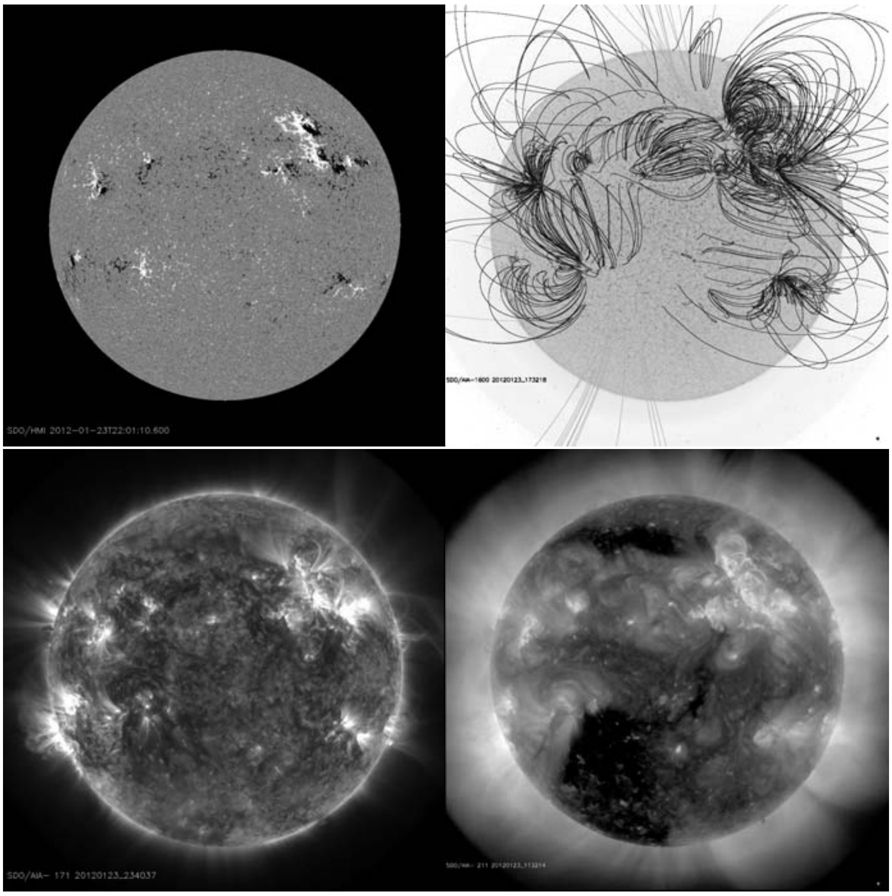

Fig. 23 A full disk HMI/SDO magnetogram (top left) with extrapolated magnetic field lines (top right), the upper TR observed in the 171 Å (Fe VIII) band (bottom left) and the corona observed in the 211 Å (Fe XIV) band (bottom right) with AIA/SDO on January 23, 2012. Images adapted from http://sdowww.lmsal.com/suntoday/

5.4 Large scale structure of the corona

The magnetic lines of force of small scale magnetic dipoles, associated with the network magnetic fields, close at relatively low heights (comparable to the distance between the opposite polarities). Thus the coronal structure is dominated by two types of magnetic configuration: one is the medium and large scale bipolar fields associated with active regions, where the plasma is confined by the magnetic field in medium and large scale loops. The other is the so called *open* magnetic configuration, associated with extended regions of the same polarity; this cannot confine the plasma, which expands in the interplanetary medium as the *fast* solar wind and what is left in the corona is just a hole. An example with both closed an open regions in the corona together with the corresponding magnetogram and extrapolated magnetic field lines is presented in Fig. 23.

As we go to heights where the solar wind attains significant speed, the kinetic energy density of the plasma increases and surpasses the energy density of the magnetic field. Thus, if a closed magnetic configuration extends high enough, the tops of the outer lines of force will be dragged by the solar wind to give rise to the magnetic configuration of a *streamer* (Fig. 24). Note that an electric current sheet (dashed line in the right panel of the figure) is formed, separating regions of opposite magnetic polarity [110]. Streamers are not cylindrically symmetric, as was thought in the past (hence the term *helmet* streamer), but go around the sun, forming a belt which is often irregular, depending on the complexity of the large scale solar magnetic field; the associated current sheets extends into the interplanetary space, forming the *heliosheet* that separates opposite magnetic polarities in the heliosphere. Streamers may also form in more complex (quadrupole) magnetic field configurations [108].

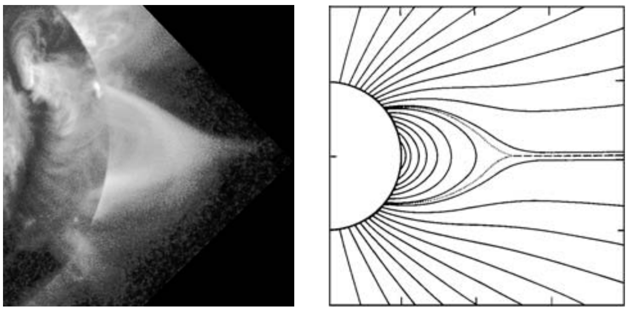

Fig. 24 A streamer observed with Yohkoh and a schematic drawing of the corresponding magnetic configuration.

The magnetic field lines of force shown in Fig. 23 have been computed under the *current-free assumption*, using the photospheric magnetic field as a lower boundary condition (Schmidt [164] in plane geometry, Altschuler and Newkirk [11] in spherical geometry and for the entire sun, see Chapter 5 in [13] for a more detailed discussion). In the more general case of the *force free* approximation, the electric current is assumed to flow along the magnetic field, so that Ampère's law, Eq. (37), takes the form:

$$\nabla \times B = \alpha B \tag{55}$$

which includes the current-free case ($\alpha = 0$). In this case the Lorentz force vanishes, hence the term force-free. It is easy to prove that α is constant along a magnetic field line. If α is assumed constant everywhere, we have the *linear* force free case; this is relatively easy to compute [3], compared to the non-linear case [13].

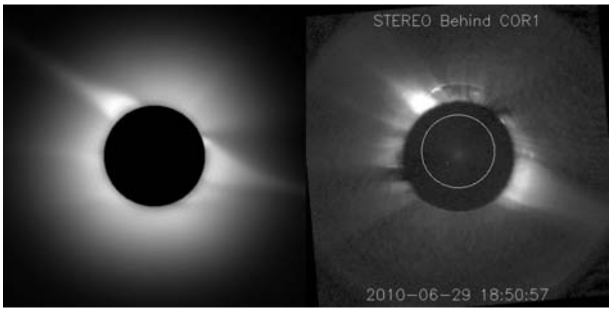

Fig. 25 Comparison of the computed intensity of the corona (left) with the corresponding image of the COR1 coronograph aboard STEREO-B, on June 29, 2010. From http://www.predsci.com/stereo/home.php

One can go further by taking into account the full set of MHD equations, and compute, in addition to the magnetic field, the density of the plasma, as well as the flow velocity in 3 dimensions. An example is shown in Fig. 25, where the coronal intensity has been computed with the MAS code [159]. Despite the fact that the computation is based on magnetic field data over a full solar rotation (26 days), the similarity with the observed corona is remarkable, in particular for large scale structures (such as streamers), which are also long-lived.

The corona is accessible with radio observations in the metric region, but here one has to be content with arc-minute resolution. Moreover, the Sun must be without any burst activity if the quiet Sun component is to be imaged. The first images were obtained with the now-extinct Culgoora Radioheliograph at 80 MHz (3.75 m) and 160 MHz (1.88 m), followed by the also extinct Clark Lake Radioheliograph at 73.8 MHz (4.07 m), 50 MHz (6 m) and 30.9 MHz (9.7 m). The Nançay Radioheliograph (NRH) operated as two independent arrays (E-W and N-S) at 169 MHz (1.78 m) until Alissandrakis, Lantos and Nicolaidis [9] employed aperture synthesis to combine 6 hours of observations into a 2D-image with $1.2'$ by $4.2'$ resolution.

The NRH has evolved gradually to its present state of 2D synthesis instrument [90], providing images at 10 frequencies from 450 to 150 MHz (67 cm to 2 m) with a cadence of 0.25 sec. The instantaneous images, however, cannot exploit the full resolution of the system since they only use the densely sampled inner part of the u-v plane. In order to exploit the full resolution one has to resort to full-day synthesis, which improves the resolution by a factor of ~ 2.5. This was done by

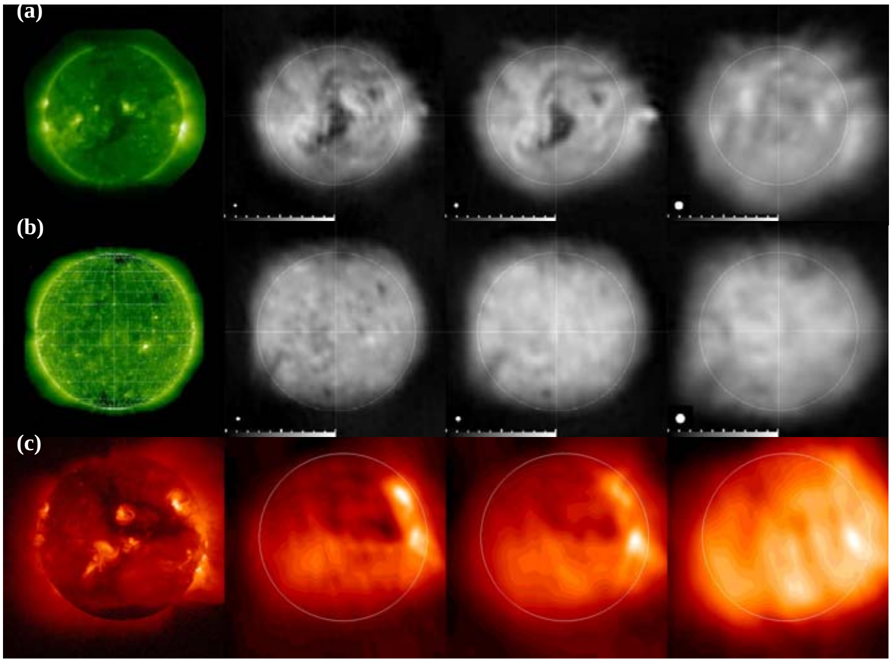

Fig. 26 Synthesis images with the Nançay Radioheliograph: (a) Images at 432, 327 and 164 MHz on June 27, 2004, together with a GOES SXI image; (b) Images at 432, 327 and 173 MHz on June 6, 2008, together with an EIT 195 Å image and (c) Images at 432, 327 and 410 MHz on May 26, 1992, together with a Yohkoh SXT image. White dots in (a) and (b) show the resolution. (a) and (b) were adapted from [132], and (c) from [116].

Marqué [129] with an emphasis on filament cavities and, more recently, by Mercier and Chambe [132, 133] in a systematic study of the quiet Sun.

Fig. 26 shows some examples of synthesis images from Mercier and Chambe [132], together with a set of 1992 images from [116]. Note that the NRH covers a broad range of frequencies, the ratio of the maximum to minimum frequency being ~ 3; it can thus probe an altitude range from the upper TR to the low corona. The altitude range goes lower in coronal holes. They are the most prominent feature at long dm wavelengths and, in agreement with previous observations (*e.g.*, Lantos *et al.* [119]), their contrast decreases at longer wavelengths.

Coronal holes are usually observed as brightness depressions at radio wavelengths (*e*.g., Lantos and Alissandrakis [117]; Borovik and Medar [30]), however at mm- and cm-waves, the average brightness temperature of coronal holes is not much different from that of the quiet Sun. A number of computations of the coronal hole radio emission (*e*.g., Borovik *et al.* [29]; Chiuderi Drago *et al.* [39], Pohjolainen [151]) have been published. Borovic *etal.* [29] observed four coronal holes in the wavelength range of 2 to 32 cm with the RATAN-600 telescope and found that the brightness difference between the holes and the quiet sun becomes appreciable after ~ 4 cm. In the best-fit models the coronal holes are cooler than the background and less dense by a factor of 2.

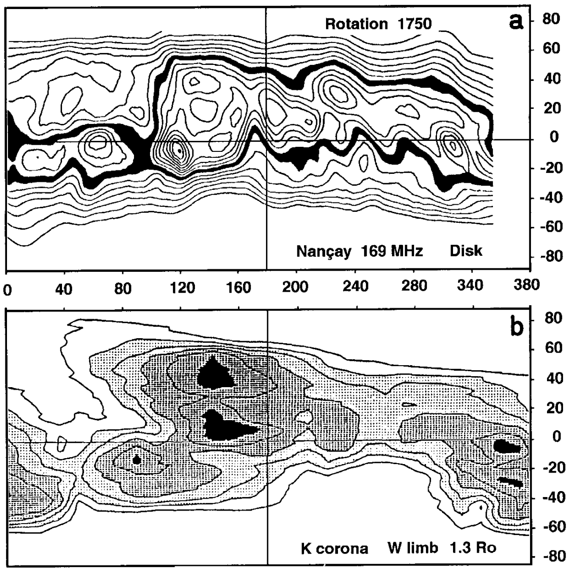

Fig. 27 (a): Synoptic map of the sun from NRH observations at 169 MHz. The black region is the *coronal plateau*. (b): The corresponding synoptic chart form K-corona observations at $1.3R_{\odot}$ on the West limb. From [118].

At decameter waves coronal holes are sometimes seen in emission, Dulk and Sheridan [49] reported such a case. Lantos *et al.* [119] observed a bright emission source at decametric wavelengths, located above an extended coronal hole, in a region where a depression was seen at meter waves. A possible interpretation is in terms of refraction effects (Alissandrakis [4], *cf* Fig. 3 of Lantos [116]) and/or scattering in inhomogeneities.

In a systematic study of emission sources observed with the NRH at 169 MHz, Lantos and Alissandrakis [117] came to the conclusion that the large scale emission is dominated by the *coronal plateau* (Fig. 27). This is an intermediate brightness area forming a belt around the Sun and surrounding almost all local emission sources (Lantos, Alissandrakis, and Rigaud [120]). It is visible both in daily images and in synoptic charts, and has a close association with the coronal plasma sheet observed with K-corona instruments (Fig. 27b). The diffuse emission of the *coronal plateau* could be due to a high altitude loop system which overrides the principal neutral line of the general solar magnetic field at the base of the heliosheet, with a possible contribution of loops connecting active regions to surrounding quiet areas. The same authors reported that medium scale local sources include both faint noise storm continua and thermal sources. Most of the latter are located between faculae and neutral lines, possibly in the upper leg of large scale loops. A small number of thermal sources is closer to neutral lines, which might be loops at the base of isolated coronal streamers.

Coronal streamers are best visible at decametric wavelengths (see Lantos [116]). They are less prominent in the meter and decimeter ranges, where one sees loops at the base of streamers rather than proper streamers, as pointed out in the previous paragraph. From the circularly polarized thermal emission of streamers observed with the Gauribidanur radioheliograph at 77 and 109 MHz, Ramesh, Kathiravan, and Sastry [154] were able to estimate magnetic field strengths in the range of 5 – 6 G at 1.5 – 1.7 solar radii.

5.5 Filaments and prominences

The configuration of the magnetic field above neutral lines of the magnetic field is such that, under certain conditions, it can sustain clouds of material of chromospheric temperature and density against gravity and thermally isolate them from the hot corona. In chromospheric lines and on the solar disk, these clouds appear in absorption as *filaments* ; projected beyond the solar disk, they appear in emission as *prominences* (see recent reviews by Labrosse *et al.* [112] and Mackay *et al.* [128]).

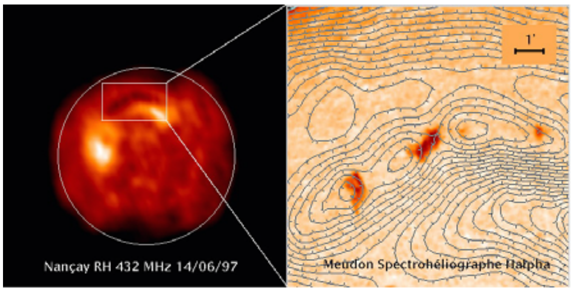

Fig. 28 Image of a filament at 432 MHz (left) and Hα (right). From [130]

At decimeter-meter wavelengths (Fig. 28), as well as in the mm and cm range (Fig. 29), large filaments are observed as regions of lower brightness temperature on the solar disk. Beyond the limb filaments are seen in emission, projected against the sky; in this case it is possible to calculate electron temperatures and densities using multi-frequency radio observations [84].

A systematic study of filaments and their environment in the metric radio range was presented by Marqué [129]. He used NRH observations primarily at at 410.5 MHz, pointing out that the visibility of filament associated radio depressions is rather poor at lower frequencies. He concluded that the most likely source of the radio depression is the cavity (electron density depletion) that surrounds the filament. Note that in cm and mm wavelengths contradictory results have been reported on the contribution of the cavity to the observed radio depression [105, 156].

A set of simultaneous observations of a filament in the microwave range and in the EUV, was analyzed by Chiuderi Drago *et al.* [38] (Fig. 29). The authors concluded that the depression at radio wavelengths is due to the lack of coronal

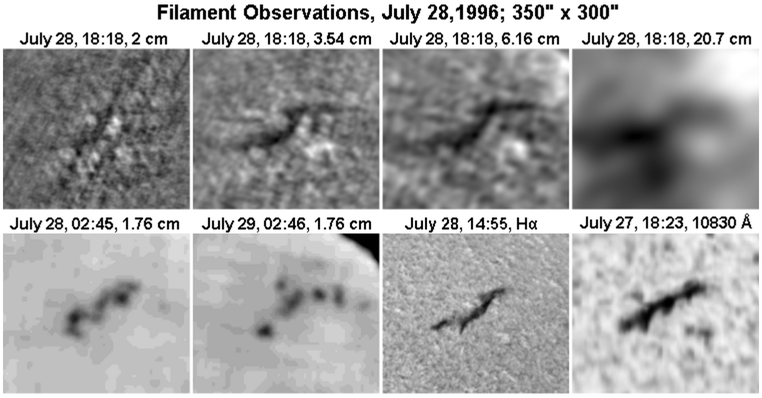

Fig. 29 A filament observed at radio wavelengths (VLA and NoRH), in Hα, and in HeI 10830Å. From data used in [38].

emission; the same data favored a prominence model with cool threads embedded in the hot coronal plasma, enveloped by a sheath-like TR, and a filling factor varying from about 3 to 4%.

6 Active Regions

Active Regions appear in the photosphere as roughly bipolar magnetic regions of intermediate scale ($\sim 0.2\mathrm{R}_\odot$, or $\sim 1.5\times10^5$ km). Sunspots, associated with strong magnetic fields (above $\sim$1000 G), are their primary manifestation in the photosphere, bright *plage* emission, associated with intermediate magnetic fields, prevails in the chromospheric layers together with elongated *fibrils*, indicating a more organized magnetic field compared to the quiet sun, while impressive loops mark their presence in the corona. They are accompanied by all sorts of dynamic phenomena, most notably flares.

Active regions are the result of emergence of large quantities of magnetic flux from the subphotospheric layers, a result of *magnetic buoyancy* (see, *e.g.* [146, 152, 157]) and disappear as the magnetic flux is dissipated in eruptive events, or is spread out as a result of convective motions. Figs. 30 and 31 show images of an active region from the photosphere to the low corona, during its emergence and development phase, as the region crosses the solar disk.

Concentrating on the radio emission, we note that in the 17 MHz images of July 30, August 2, 3 and 4 show the classic two components of sunspot and plage associated emission, identified for the first time by Kundu [100] with a 2-element interferometer and imaged by Kundu and Alissandrakis [102] with the Westerbork Synthesis Radio Telescope. Since that time many observations have been published (see reviews by Gelfreikh [71] and Lee [121]). It is well established that the sunspot,

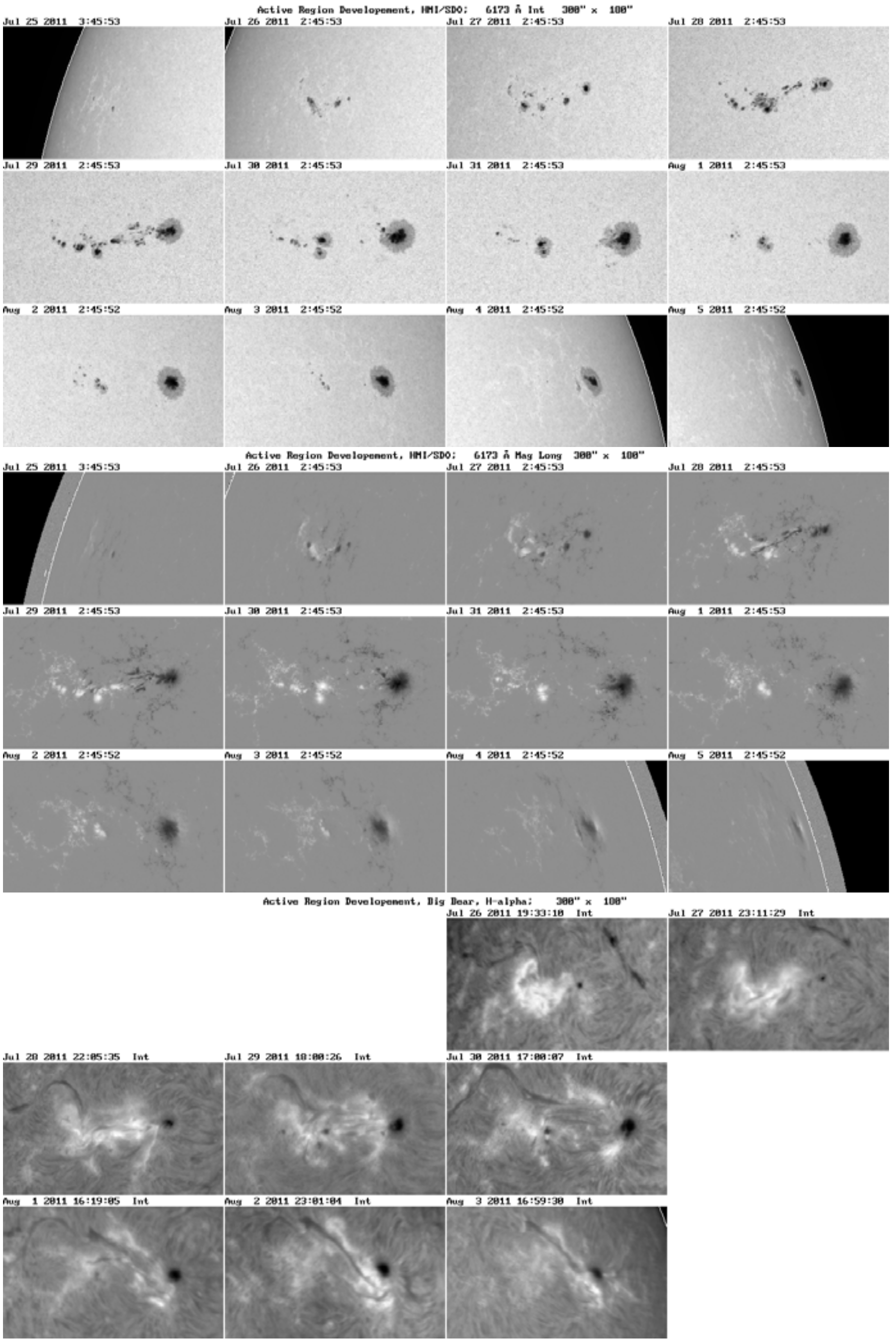

Fig. 30 Development of Active Region 11260 during its passage on the solar disk. Sunspots and magnetograms from HMI/SDO, Hα images from Big Bear. Note that the Hα images were taken a few hours before the others. The region crossed the central meridian on July 30, $\sim$9 UT. The white line marks the photospheric limb

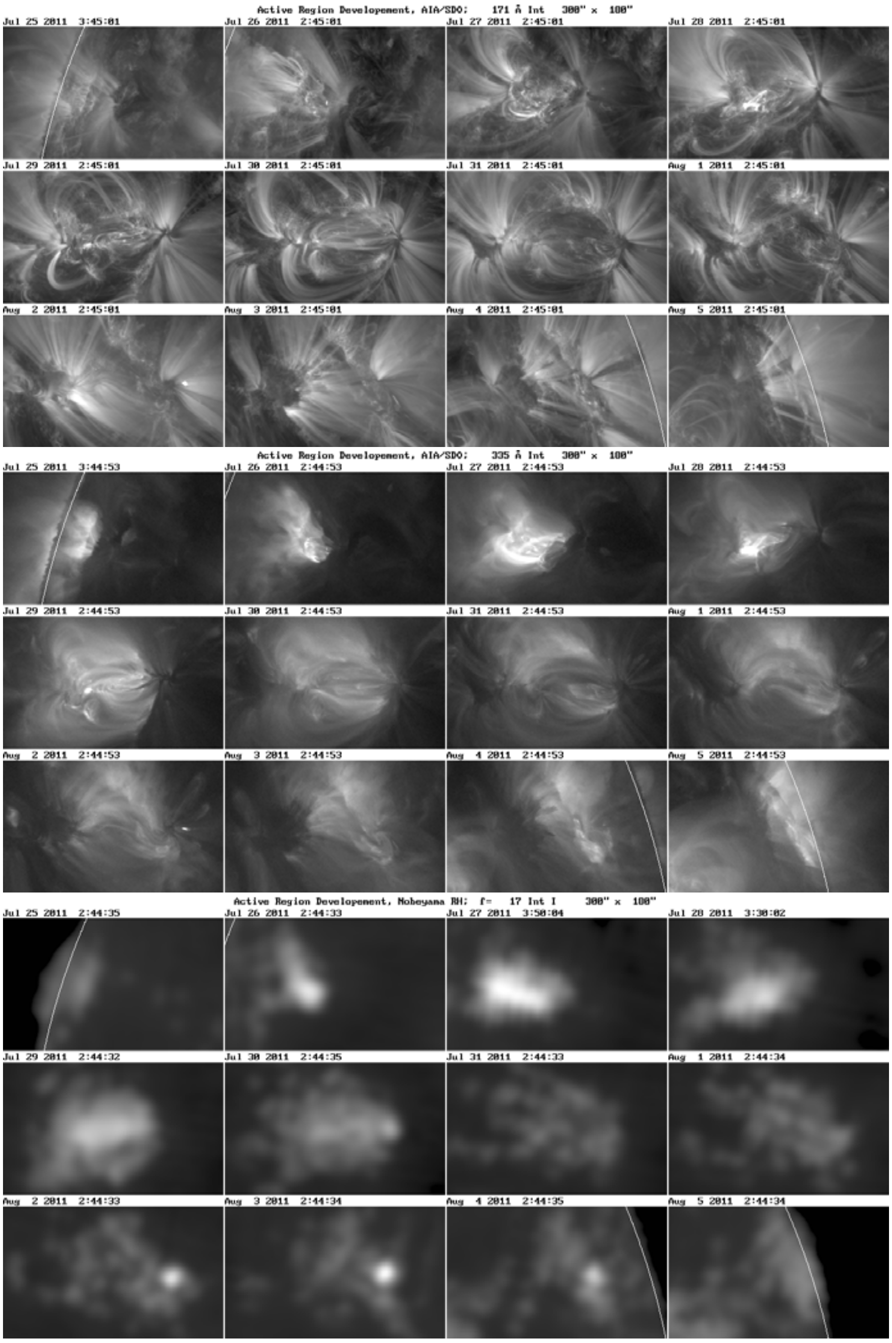

Fig. 31 Same as Fig. 30, in the 171 Å band (Fe IX, $\log T \sim 5.8$), in the 335 Å band (Fe XVI, $\log T \sim 6.4$) from AIA/SDO and at 17 GHz from the NoRH

or core component of the emission is due to the gyroresonance process [88, 196, 8], whereas the plage, or halo component is due to free-free emission (see also chapter by Nindos).

Going back to Figs. 30 and 31, note that no sunspot component is visible on the other days, apparently due to the low value of the sunspot field with regard to the observing frequency. Note also that on July 26 to 28, emission as strong as the sunspot emission is observed, apparently associated with hot coronal loops seen in the 335 Å, (Fe XVI) band. This is reminiscent of the *neutral line sources* reported by Kundu *et al.* [104] (see also [182] and references therein) and attributed to a quasi-steady, low density population of non-thermal electrons [10].

At longer wavelengths a *decimetric halo component* of non-thermal nature has been reported [71], while at even longer decimetric and metric wavelengths no sunspot-associated emission is visible, presumably due to the high opacity of the overlaying plasma and refraction effects.

The microwave emission of active regions is a powerful diagnostic of the magnetic field in the transition region and the low corona. The magnetic field determines the emissivity of gyroresonace process operating above sunspots, of the free-free process above plages, as well as polarization inversion effects higher up (see the relevant chapter in this book for details).

In addition to the magnetic field, sunspot-associated emission can provide information about the temperature and density structure of the sunspot atmosphere [139, 92]. In this context, it is interesting to mention the detection of low temperature material in the corona above certain sunspots [7, 177], which was interpreted as the radio counterpart of cool sunspot plumes embedded in the hot corona and detected in the EUV by Skylab [64, 65] This was later verified by Brosius and White [33], from simultaneous microwave and EUV observations. Let us also mention in passing the detection and study of sunspot oscillations [73, 140] and refer the reader to the review by Nindos and Aurass [138] for more details. We also refer the reader to the reviews by Solanki [173] and by Rempel and Schlichenmaier [157] for extensive descriptions of sunspots.

7 Heating of the Chromosphere and the Corona

7.1 The problem

Elementary thermodynamics tells us that you cannot transfer energy from a cold body to a hot body through radiation, conduction or convection. How do you then explain the temperature minimum and the subsequent temperature rise in the chromosphere and the corona and the energy carried away by the solar wind? The obvious answer is that you have to transport energy from below by mechanical means.

The first answer was proposed more than 60 years ago, by Schwarzschild [163] and by Schatzman [162]: the chromosphere and the corona are heated by the dissipation of shock waves, originating as acoustic waves in the the noise produced by the granulation and steepened as they propagate upwards in regions of decreasing density. The discovery of the five-minute oscillations gave a boost to this idea, still other ideas, more promising, have been advanced. In what follows we will discuss some concepts and constrains with regard to the heating problem. Obviously, we cannot be exhaustive, so we refer the reader to Chapter 6 of Priest [152], Chapter 9 of Aschwanden [13] and reviews by Withbroe and Noyes [191], Walsh and Ireland [188], Klimchuk [91] and Erdélyi and Ballai [53].

First of all, the question is not that of bulk heating, as the upper solar atmosphere is highly structured (Section 5). In the chromosphere, for example, we need to supply more energy to the network, which is brighter, more dense and more dynamic than the internetwork regions. In the corona, individual flux tubes have their own energy requirements. A loop will become visible in a particular spectral line, if it contains enough plasma at the appropriate temperature; this plasma presumably comes from the chromosphere, through evaporation induced by the deposition of energy somewhere in the loop. Open flux tubes in coronal holes must also be heated, both on their own sake and in order to provide energy to the plasma that makes the fast solar wind. Note also that coronal heating requirements vary during the solar cycle, as evidenced by the great variations in X-ray brightness revealed by Yohko images. Thus the problem is not just to have an abundance of wave or some other form of mechanical energy, but mainly to transport and dissipate the energy at the proper place and at the proper time.

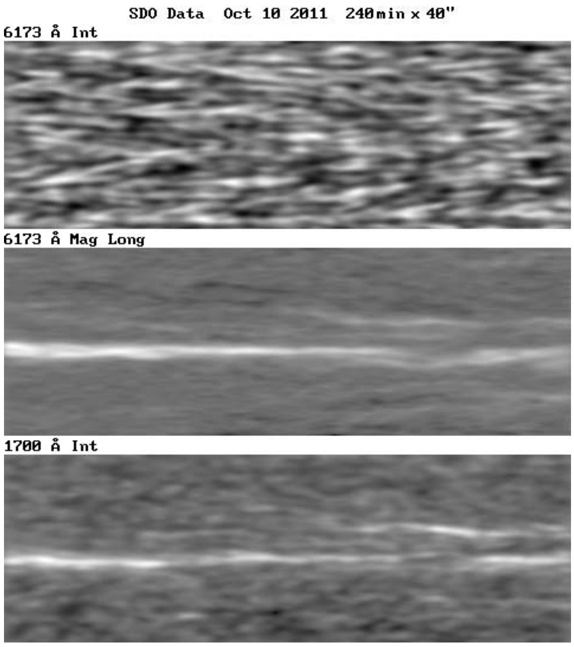

Fig. 32 Position (vertical axis) - time (horizontal axis) cuts through a magnetic element. Granular motions are clearly visible in the top panel; the middle and the bottom panels show the motion of the magnetic element and the corresponding bright point in the 1700 Å band. A low pass filter has been applied in the time domain to reduce the effect of the 5 minute oscillations.

The magnetic field plays the primary role in determining the structure of the upper atmospheric (Section 5); we also expect the magnetic field to influence the propagation of acoustic waves and, in addition, to provide plenty of additional wave modes. Wave heating, which is commonly referred to as *AC heating*, is not the only possibility. At the photospheric level, magnetic flux tubes (section 5.3) are known to be in continuous motion, as shown in Fig. 32, in response to horizontal convective flows. As a result waves could be excited but, what is probably more important, the magnetic lines of force, which extend up in the chromosphere and the corona, will become tangled, accumulating magnetic energy in innumerable current sheets. This magnetic energy cannot accumulate *in perpetuo*, thus it will eventually be converted to heat (*DC heating*) in the course of reconnection, either through Joule dissipation (Eq. 51), or even through collisionless processes. Note that these processes could also accelerate particles that will eventually depose their energy in the plasma; these particles should have observable consequences both in the radio and the hard X-ray range.

Reconnection mechanisms have been invoked to explain energy release in flares, hence the concept of *nanoflare heating*, first proposed by Parker [148]. Nanoflares are impulsive by nature and are expected to occur in elemental flux tubes that are below the resolution limit of present-day instruments. Impulsiveness is not limited to nanoflares, but may characterize AC heating as well [91].

A radically different approach has been advanced by Scudder [165], that the coronal plasma originates in suprathermal particles escaping from the transition region. A common criticism to this idea [91] is that, if it were correct, the corona should be similar in the quiet Sun and coronal holes, since the transition region is quite similar in these regions (see bottom images in Fig 23).

Although we have plenty of mechanisms, we have no answer as to which mechanism(s) may operate and in which case. As a matter of fact, we have plenty of negative answers. It is encourging that there is sufficient energy associated with the granulation noise, as already pointed out by Schatzman and also in the random motion of magnetic flux tubes [91, 6], but this is not enough, as pointed up above. Nanoflare heating is certainly attractive, but it evades observational confirmation. Several authors have computed histograms of the energy distribution in impulsive events, including microflares observed in abundance with RHESSI and previous missions [81]; the extrapolation to low energies only gave negative results as far as heating is concerned. Acoustic wave heating has been a favorite for the non-magnetic chromosphere, but it appears that the appropriate waves do not carry enough energy [63]. Other types of waves, such as Alfvén waves in the presence of turbulence [183], might help.

Let us finally note that, in addition to heating the upper chromosphere, one has to replenish the corona with the mass lost through the solar wind. However, this is not considered a problem since, as it has been shown a long time ago [24], spicules that diffuse into the corona carry more mass than is actually required.

7.2 Pertinent radio data

We will now summarize radio observations that might have a bearing to the heating problem (see also [6] and [169]). It is fairly well established [54, 20] that radio fine structures show time variability comparable to that of the chromospheric network, on time scales of minutes to hours. Apart from that, it is important to check for oscillatory behavior, which could be a signature of shock waves heating the upper solar atmosphere. This is not an easy task, due to the inherent difficulties in the instantaneous mapping of complex structures. In this context, White, Loukitcheva and Solanki [190] reported intensity oscillations in the mm-wavelength range with rms brightness variation of 50-150 K; they noted that network regions had a tendency to exhibit longer period oscillations than the intranetwork.

A number of authors have looked for impulsive/transient events that may have a bearing on the heating of the upper atmosphere, as the radio range is very sensitive to small non-thermal electron populations that are expected as a by-product of the reconnection process. In this context, Krucker *et al.* [98] detected four Yohkoh soft X-ray events associated with radio emission at 2 cm in 10 s VLA snapshot images; they estimated that roughly one such event occurs on the Sun every 3 seconds, all together providing a total power of $\sim 2\times 10^{25}$ erg s^{-1}, which is 5 times less than the total power radiated by the quiet corona in X-rays. In a similar study Gary, Hartl and Shimizu [68], using one OVRO antenna and Yohkoh SXT images, found that only 5 out of 35 transient brightenings detected with SXT in an active region had no radio counterpart; they also found a delay of 1 to 2 min of the X-ray peak with respect to the radio. The relative timing of events was also studied by Benz and Krucker [27], using data at 2, 3.6, and 6 cm from VLA together with EIT, CDS and SUMER data from SOHO. They found that the radio peaks preceded the coronal emission and lagged behind O V emission (see also [97]).

Some of these transient events have flare-like characteristics and might be associated with X-ray bright points rather than with the network proper. Indeed, there appears to be a continuity between bursts, the radio counterparts of X-ray bright points (see Keller and Krucker [89] and references therein), and smaller events such as those described in the previous paragraph. Transient brightenings are observed in microwaves both within and well-away from any active region and both thermal and non-thermal emission mechanisms have been suggested [189, 141]. In any case, it seems evident that electrons are accelerated to non-thermal energies even in the quiet solar atmosphere.

At longer wavelengths, short-duration, isolated metric radio bursts, not associated with any radio continuum and located outside active regions have been reported [41, 153]. Burst locations were determined from radioheliograph images, but no counterparts were found in X-ray, EUV, and UV events. Further analysis would require simultaneous high time-resolution imaging data at all wavelengths. Decametric radio observations present numerous faint, frequency-drifting emissions, similar to "solar S bursts" reported by McConnell [131]. No specific relationship between the occurrence of these emissions and the solar cycle or presence of flares have been found by Briand *et al.* [32], who suggested that a moderate, localized, timedependent heating leads to low velocity electron clouds, which can in turn generate Langmuir waves and electromagnetic signals by nonlinear processes.

We may conclude that radio observations can provide important input to the problem of the heating of the chromosphere and the corona, both in the wave and nanoflare heating scenarios. Instruments with dense coverage of the u-v plane as well as improved reconstruction techniques are necessary, in order to provide accurate instantaneous images of regions with complex structure.

8 Final comments

In addition to being our source of life, the sun is also the nearest star (hence the stellar prototype) and an immense laboratory of plasma physics. During the last few decades we have accumulated a tremendous amount of knowledge on how the sun operates and how it affects our daily life, thanks to the development of new instruments, both ground-based and space-born, and the advances in the theory and numerical simulations.

An important ingredient of the recent progress is the exploitation of information from all spectral ranges. The radio domain is a basic source of information. In this respect, it is in competition with the EUV and X-ray domains which also provide information about the same layers of the solar atmosphere and the same phenomena. We should stress. however, that the interpretation of radio data, at least for the quiet sun and a good part of active phenomena, is straight forward; it is not plagued by non-LTE effects, uncertainties in excitation and ionization equilibrium and abundances, as are other wavelength ranges. The weakness of radio is the low spatial resolution, but this can be overcome with large synthesis instruments, without having to go to to space; there are several such projects under development (see Section 6.2 in [169]).

As it is usually the case, as we learn more, old questions are answered, at least partially, and new questions emerge. With the new instrumentation currently under development and the continued effort on the theoretical side, we will certainly have important results in the next few years.

Acknowledgements

References

1. Ahmad, Q.R., Allen, R.C., Andersen, T.C., and 176 coauthors: 2002, *Physical Review Letters* **89**, 011301.
2. Allen, C.W.: 1947, *Monthly Notices of the Royal Astronomical Society* **107**, 426.
3. Alissandrakis, C.E.: 1981, *Astron. Astroph.* **100**, 197.
4. Alissandrakis, C.E.: 1994, *Advances in Space Research* **14**, 81.
5. Alissandrakis, C.E., Dialetis, D., and Tsiropoula, G.: 1987, *Astron. Astroph.* **174**, 275.
6. Alissandrakis, C.E. and Einaudi, G.: 1997, *Lecture Notes in Physics* **483**, 53.
7. Alissandrakis, C.E. and Kundu, M.R.: 1982, *Astrophys. J.* **253**, L49.
8. Alissandrakis, C.E., Kundu, M.R., and Lantos, P.: 1980, *Astron. Astroph.* **82**, 30.
9. Alissandrakis, C.E., Lantos, P., and Nicolaidis, E.: 1985, *Solar Phys.* **97**, 267.
10. Alissandrakis, C.E., Gel'Frejkh, G.B., Borovik, V.N., Korzhavin, A.N., Bogod, V.M., Nindos, A., and Kundu, M.R.: 1993, *Astron. Astroph.* **270**, 509.
11. Altschuler, M.D. and Newkirk, G.: 1969, *Solar Phys.* **9**, 131.
12. Appourchaux, T., Belkacem, K., Broomhall, A.-M., Chaplin, W.J., Gough, D.O., Houdek, G., Provost, J., Baudin, F., Boumier, P., Elsworth, Y., García, R.A., Andersen, B.N., Finsterle, W., Fröhlich, C., Gabriel, A., Grec, G., Jiménez, A., Kosovichev, A., Sekii, T., Toutain, T., and Turck-Chièze, S.: 2010, *Astronomy and Astrophysics Review* **18**, 197.
13. Aschwanden, M.J.: 2004, *Physics of the Solar Corona*.
14. Asplund, M., Grevesse, N., Sauval, A.J., and Scott, P.: 2009, *Annual Review of Astronomy and Astrophysics* **47**, 481.
15. Athay, R.G.: 1971, *Physics of the Solar Corona* **27**, 36.
16. Aubier, M., Leblanc, Y., and Boischot, A.: 1971, *Astron. Astroph.* **12**, 435.
17. Avrett, E.H.: 1995, *Proc. 15th NSO Sac Peak Workshop, Infrared Tools for Solar Astrophysics: What's Next?*, 303.
18. Avrett, E.H. and Loeser, R.: 2008, *The Astrophysical Journal Supplement Series* **175**, 229.
19. Bastian, T.S.: 1994, *Astrophys. J.* **426**, 774.
20. Bastian, T.S., Dulk, G.A., and Leblanc, Y.: 1996, *Astrophys. J.* **473**, 539.
21. Basu, S., Christensen-Dalsgaard, J., Chaplin, W.J., Elsworth, Y., Isaak, G.R., New, R., Schou, J., Thompson, M.J., and Tomczyk, S.: 1997, *Monthly Notices of the Royal Astronomical Society* **292**, 243.
22. Baudin, F., Molowny-Horas, R., and Koutchmy, S.: 1997, *Astron. Astroph.* **326**, 842.
23. Beckers, J.M.: 1968, *Solar Phys.* **3**, 367.
24. Beckers, J.M.: 1972, *Annual Review of Astronomy and Astrophysics* **10**, 73.
25. Belkora, L., Hurford, G.J., Gary, D.E., and Woody, D.P.: 1992, *Astrophys. J.* **400**, 692.
26. Benz, A.O., Krucker, S., Acton, L.W., and Bastian, T.S.: 1997, *Astron. Astroph.* **320**, 993.
27. Benz, A.O. and Krucker, S.: 1999, *Astron. Astroph.* **341**, 286.
28. Bogod, V.M. and Korolkov, D.V.: 1975, *Soviet Astronomy Letters* **1**, 205.
29. Borovik, V. N., Kurbanov, M. S., Livshits, M. A., Ryabov, B. I.: 1990, *Astron. Zh.* **67**, 1038 (*Sov. Astron.* **34**, 522).
30. Borovik, V.N. and Medar, V.G.: 1999, *8th SOHO Workshop: Plasma Dynamics and Diagnostics in the Solar Transition Region and Corona* **446**, 185.
31. Bray, R.J. and Loughhead, R.E.: 1967, The solar granulation, *The International Astrophysics Series, London: Chapman & Hall, 1967*.
32. Briand, C., Zaslavsky, A., Maksimovic, M., Zarka, P., Lecacheux, A., Rucker, H.O., Konovalenko, A.A., Abranin, E.P., Dorovsky, V.V., Stanislavsky, A.A., and Melnik, V.N.: 2008, *Astron. Astroph.* **490**, 339.
33. Brosius, J.W. and White, S.M.: 2004, *Astrophys. J.* **601**, 546.
34. Brown, T.M., Stebbins, R.T., and Hill, H.A.: 1978, *Astrophys. J.* **223**, 324.
35. Carlsson, M.: 2007, *The Physics of Chromospheric Plasmas* **368**, 49.
36. Charbonneau, P.: 2010, *Living Reviews in Solar Physics* **7**, 3.
37. Chiuderi Drago, F., Kundu, M.R., and Schmahl, E.J.: 1983, *Solar Phys.* **85**, 237.

38. Chiuderi Drago, F., Alissandrakis, C.E., Bastian, T., Bocchialini, K., and Harrison, R.A.: 2001, *Solar Phys.* **199**, 115.
39. Chiuderi Drago, F., Landi, E., Fludra, A., and Kerdraon, A.: 1999, *Astron. Astroph.* **348**, 261.
40. Christensen-Dalsgaard, J.: 2002, *Reviews of Modern Physics* **74**, 1073.
41. Crosby, N., Vilmer, N., Chiuderi Drago, F., Pick, M., Kerdraon, A., Khan, J., and Schwenn, R.: 1997, *Fifth SOHO Workshop: The Corona and Solar Wind Near Minimum Activity* **404**, 299.
42. Davis, R.: 2003, *Reviews of Modern Physics* **75**, 985.
43. Dara, H.C., Alissandrakis, C.E., and Koutchmy, S.: 1987, *Solar Phys.* **109**, 19.
44. De Pontieu, B., Erdélyi, R., and James, S.P.: 2004, *Nature* **430**, 536.
45. Deubner, F.-L.: 1975, *Astron. Astroph.* **44**, 371.
46. de Pontieu, B., McIntosh, S., Hansteen, V.H., Carlsson, M., Schrijver, C.J., Tarbell, T.D., Title, A.M., Shine, R.A., Suematsu, Y., Tsuneta, S., Katsukawa, Y., Ichimoto, K., Shimizu, T., and Nagata, S.: 2007, *Publications of the Astronomical Society of Japan* **59**, 655.
47. de Wijn, A.G., Stenflo, J.O., Solanki, S.K., and Tsuneta, S.: 2009, *Space Science Reviews* **144**, 275.
48. Dunn, R.B. and Zirker, J.B.: 1973, *Solar Phys.* **33**, 281.
49. Dulk, G.A. and Sheridan, K.V.: 1974, *Solar Phys.* **36**, 191.
50. Dupree, A.K. and Goldberg, L.: 1967, *Solar Phys.* **1**, 229.
51. Durrant, C.J.: 1988, The atmosphere of the sun *Bristol: Hilger, 1988*.
52. Edlén, B.: 1943, *Zeitschrift fur Astrophysik* **22**, 30.
53. Erdélyi, R. and Ballai, I.: 2007, *Astronomische Nachrichten* **328**, 726.
54. Erskine, F.T. and Kundu, M.R.: 1982, *Solar Phys.* **76**, 221.
55. Evans, J.W. and Michard, R.: 1962, *Astrophys. J.* **136**, 493.
56. Fontenla, J.M., Avrett, E.H., and Loeser, R.: 1990, *Astrophys. J.* **355**, 700.
57. Fontenla, J.M., Avrett, E.H., and Loeser, R.: 1991, *Astrophys. J.* **377**, 712.
58. Fontenla, J.M., Avrett, E.H., and Loeser, R.: 1993, *Astrophys. J.* **406**, 319.
59. Fontenla, J.M., Avrett, E.H., and Loeser, R.: 2002, *Astrophys. J.* **572**, 636.
60. Fontenla, J.M., Avrett, E., Thuillier, G., and Harder, J.: 2006, *Astrophys. J.* **639**, 441.
61. Fontenla, J.M., Balasubramaniam, K.S., and Harder, J.: 2007, *Astrophys. J.* **667**, 1243.
62. Fontenla, J.M., Curdt, W., Haberreiter, M., Harder, J., and Tian, H.: 2009, *Astrophys. J.* **707**, 482.
63. Fossum, A. and Carlsson, M.: 2005, *Nature* **435**, 919.
64. Foukal, P.V., Noyes, R.W., Reeves, E.M., Schmahl, E.J., Timothy, J.G., Vernazza, J.E., Wilhbroe, G.L., and Huber, M.C.E.: 1974, *Astrophys. J.* **193**, L143.
65. Foukal, P.V.: 1976, *Astrophys. J.* **210**, 575.
66. Foukal, P.V.: 2004, *Solar Astrophysics, 2nd, Revised Edition. ISBN 3-527-40374-4. Wiley-VCH*.
67. Gary, D.E.: 1996, *ASP Conf. Series* **93**, 387.
68. Gary, D.E., Hartl, M.D., and Shimizu, T.: 1997, *Astrophys. J.* **477**, 958.
69. Gary, D.E. and Zirin, H.: 1988, *Astrophys. J.* **329**, 991.
70. Gary, D.E., Zirin, H., and Wang, H.: 1990, *Astrophys. J.* **355**, 321.
71. Gelfreikh, G.B.: 1998, *ASP Conf. Series* **155**, 110.
72. Gelfreikh, G.B., Kaidanovskii, M.N., Kononovich, E.V., Smirnova, O.B., Stotskii, A.A., and Trushkin, S.A.: 1977, *Pis ma Astronomicheskii Zhurnal* **3**, 550 (*Soviet Astronomy Letters* **3**, 300).
73. Gelfreikh, G.B., Grechnev, V., Kosugi, T., and Shibasaki, K.: 1999, *Solar Phys.* **185**, 177.
74. Gelfreikh, G.B. and Lubyshev, B.I.: 1979, *Astronomicheskii Zhurnal* **56**, 562 (*Soviet Astronomy* **23**, 316).
75. Gingerich, O. and de Jager, C.: 1968, *Solar Phys.* **3**, 5.
76. Gingerich, O., Noyes, R.W., Kalkofen, W., and Cuny, Y.: 1971, *Solar Phys.* **18**, 347.
77. Gizon, L., Birch, A.C., and Spruit, H.C.: 2010, *Annual Review of Astronomy and Astrophysics* **48**, 289.

78. Gizon, L., Schunker, H., Baldner, C.S., Basu, S., Birch, A.C., Bogart, R.S., Braun, D.C., Cameron, R., Duvall, T.L., Hanasoge, S.M., Jackiewicz, J., Roth, M., Stahn, T., Thompson, M.J., and Zharkov, S.: 2009, *Space Science Reviews* **144**, 249.
79. Grotian, W.: 1939, *Naturwissenschaften* **27**, 214.
80. Habbal, S.R. and Gonzalez, R.D.: 1991, *Astrophys. J.* **376**, L25.
81. Hannah, I.G., Hudson, H.S., Battaglia, M., Christe, S., Kašparová, J., Krucker, S., Kundu, M.R., and Veronig, A.: 2011, *Space Science Reviews* **159**, 263.
82. Heintze, J.R.W., Hubenet, H., and de Jager, C.: 1964, *SAO Special Report* **167**, 240.
83. Hoang, S. and Steinberg, J.L.: 1977, *Astron. Astroph.* **58**, 287.
84. Irimajiri, Y., Takano, T., Nakajima, H., Shibasaki, K., Hanaoka, Y., and Ichimoto, K.: 1995, *Solar Phys.* **156**, 363.
85. Jackiewicz, J., Gizon, L., and Birch, A.C.: 2008, *Solar Phys.* **251**, 381.
86. Judge, P.G. and Carlsson, M.: 2010, *Astrophys. J.* **719**, 469.
87. Ishikawa, R. and Tsuneta, S.: 2011, *Astrophys. J.* **735**, 74.
88. Kakinuma, T. and Swarup, G.: 1962, *Astrophys. J.* **136**, 975.
89. Keller, C. U. and Krucker, S.: 2004, Radio Observations of the Quiet Sun. In: Gary, D. E. and Keller, C. U. (eds.) *Solar and Space Weather Radiophysics*, Kluwer Academic Publishers, 287.
90. Kerdraon, A. and Delouis, J.-M.: 1997, *Coronal Physics from Radio and Space Observations* **483**, 192.
91. Klimchuk, J.A.: 2006, *Solar Phys.* **234**, 41.
92. Korzhavin, A.N., Opeikina, L.V., and Peterova, N.G.: 2010, *Astrophysical Bulletin* **65**, 60.
93. Kosovichev, A.G.: 2011, *ArXiv e-prints*, arXiv:1103.1707.
94. Kosovichev, A.G. and Duvall, T.L., Jr.: 1997, *SCORe'96 : Solar Convection and Oscillations and their Relationship* **225**, 241.
95. Krissinel, B.B.: 2005, *Astronomy Reports* **49**, 939.
96. Kuiper, G.P.: 1953, *The Sun*.
97. Krucker, S. and Benz, A.O.: 2000, *Solar Phys.* **191**, 341.
98. Krucker, S., Benz, A.O., Bastian, T.S., and Acton, L.W.: 1997, *Astrophys. J.* **488**, 499.
99. Krüger, A.: 1979, *Geophysics and Astrophysics Monographs, Dordrecht: Reidel, 1979*.
100. Kundu, M.R.: 1959, *Annales d'Astrophysique* **22**, 1.
101. Kundu, M.R.: 1965, *Solar radio astronomy*, Interscience Publication, New York.
102. Kundu, M.R. and Alissandrakis, C.E.: 1975a, *Nature* **257**, 465.
103. Kundu, M. R. and Alissandrakis, C. E.: 1975b, *MNRAS* **173**, 65.
104. Kundu, M.R., Alissandrakis, C.E., Bregman, J.D., and Hin, A.C.: 1977, *Astrophys. J.* **213**, 278.
105. Kundu, M.R. and McCullough, T.P.: 1972, *Solar Phys.* **24**, 133.
106. Kundu, M.R., Rao, A.P., Erskine, F.T., and Bregman, J.D.: 1979, *Astrophys. J.* **234**, 1122.
107. Kundu, M.R. and Velusamy, T.: 1974, *Solar Phys.* **34**, 125.
108. Koutchmy, S., Koutvitsky, V.A., Molodensky, M.M., Solov'iev, L.S., and Koutchmy, O.: 1994, *Space Science Reviews* **70**, 283.
109. Koutchmy, S.: 1994, *Advances in Space Research* **14**, 29.
110. Koutchmy, S. and Livshits, M.: 1992, *Space Science Reviews* **61**, 393.
111. Koutchmy, S.: 1972, *Solar Phys.* **24**, 373.
112. Labrosse, N., Heinzel, P., Vial, J.-C., Kucera, T., Parenti, S., Gunár, S., Schmieder, B., and Kilper, G.: 2010, *Space Science Reviews* **151**, 243.
113. Landi, E. and Chiuderi Drago, F.: 2003, *Astrophys. J.* **589**, 1054.
114. Landi, E. and Chiuderi Drago, F.: 2008, *Astrophys. J.* **675**, 1629.
115. Lantos, P., Kundu, M. R.: *Astron. Astroph.*, **21**, 119.
116. Lantos, P.: 1999, *Proceedings of the Nobeyama Symposium*, NRO Report 479, 11.
117. Lantos, P. and Alissandrakis, C.E.: 1999, *Astron. Astroph.* **351**, 373.
118. Lantos, P. and Alissandrakis, C.E.: 1996, *Solar Phys.* **165**, 83.
119. Lantos, P., Alissandrakis, C.E., Gergely, T., and Kundu, M.R.: 1987, *Solar Phys.* **112**, 325.
120. Lantos, P., Alissandrakis, C.E., and Rigaud, D.: 1992, *Solar Phys.* **137**, 225.
121. Lee, J.: 2007, *Space Science Reviews* **133**, 73.

122. Leighton, R.B., Noyes, R.W., and Simon, G.W.: 1962, *Astrophys. J.* **135**, 474.
123. Lites, B.W., Kubo, M., Socas-Navarro, H., Berger, T., Frank, Z., Shine, R., Tarbell, T., Title, A., Ichimoto, K., Katsukawa, Y., Tsuneta, S., Suematsu, Y., Shimizu, T., and Nagata, S.: 2008, *Astrophys. J.* **672**, 1237.
124. Loukitcheva, M., Solanki, S.K., and White, S.: 2006, *Astron. Astroph.* **456**, 713.
125. Loukitcheva, M., Solanki, S.K., and White, S.M.: 2009, *Astron. Astroph.* **497**, 273.
126. Loukitcheva, M., Solanki, S.K., and White, S.M.: 2010, *Memorie della Societa Astronomica Italiana* **81**, 592.
127. Lynch, D.K., Beckers, J.M., and Dunn, R.B.: 1973, *Solar Phys.* **30**, 63.
128. Mackay, D.H., Karpen, J.T., Ballester, J.L., Schmieder, B., and Aulanier, G.: 2010, *Space Science Reviews* **151**, 333.
129. Marqué, C.: 2004, *Astrophys. J.* **602**, 1037.
130. Marqué, C., Lantos, P., Delouis, J.M., and Alissandrakis, C.E.: 1999, *8th SOHO Workshop: Plasma Dynamics and Diagnostics in the Solar Transition Region and Corona* **446**, 483.
131. McConnell, D.: 1982, *Solar Phys.* **78**, 253.
132. Mercier, C. and Chambe, G.: 2009, *Astrophys. J.* **700**, L137.
133. Mercier, C. and Chambe, G.: 2012, *Astrophys. J. in press*.
134. Mihalas, D.: 1970, Stellar Atmospheres *Series of Books in Astronomy and Astrophysics, San Francisco: Freeman, —c1970*.
135. Moradi, H., Baldner, C., Birch, A.C., Braun, D.C., Cameron, R.H., Duvall, T.L., Gizon, L., Haber, D., Hanasoge, S.M., Hindman, B.W., Jackiewicz, J., Khomenko, E., Komm, R., Rajaguru, P., Rempel, M., Roth, M., Schlichenmaier, R., Schunker, H., Spruit, H.C., Strassmeier, K.G., Thompson, M.J., and Zharkov, S.: 2010, *Solar Phys.* **267**, 1.
136. Newkirk, G., Jr.: 1961, *Astrophys. J.* **133**, 983.
137. Newkirk, G., Jr.: 1967, *Annual Review of Astronomy and Astrophysics* **5**, 213.
138. Nindos, A. and Aurass, H.: 2007, *Lecture Notes in Physics, Berlin Springer Verlag* **725**, 251.
139. Nindos, A., Alissandrakis, C.E., Gelfreikh, G.B., Borovik, V.N., Korzhavin, A.N., and Bogod, V.M.: 1996, *Solar Phys.* **165**, 41.
140. Nindos, A., Alissandrakis, C.E., Gelfreikh, G.B., Bogod, V.M., and Gontikakis, C.: 2002, *Astron. Astroph.* **386**, 658.
141. Nindos, A., Kundu, M.R., and White, S.M.: 1999, *Astrophys. J.* **513**, 983.
142. Nordlund, Å., Stein, R.F., and Asplund, M.: 2009, *Living Reviews in Solar Physics* **6**, 2.
143. Noyes, R.W., Beckers, J.M., and Low, F.J.: 1968, *Solar Phys.* **3**, 36.
144. November, L.J., Toomre, J., Gebbie, K.B., and Simon, G.W.: 1981, *Astrophys. J.* **245**, L123.
145. Ossendrijver, M.: 2003, *Astronomy and Astrophysics Review* **11**, 287.
146. Parker, E.N.: 1955, *Astrophys. J.* **121**, 491.
147. Parker, E.N.: 1978, *Astrophys. J.* **221**, 368.
148. Parker, E.N.: 1988, *Astrophys. J.* **330**, 474.
149. Pasachoff, J.M., Jacobson, W.A., and Sterling, A.C.: 2009, *Solar Phys.* **260**, 59.
150. Pikel'Ner, S.B.: 1969, *Astronomicheskii Zhurnal* **46**, 328.
151. Pohjolainen, S.: 2000, *Astron. Astroph.* **361**, 349.
152. Priest, E.R.: 1987, *Solar magneto-hydrodynamics*. Dordrecht: D. Reidel, 1987..
153. Ramesh, R., Kathiravan, C., Barve, I.V., Beeharry, G.K., and Rajasekara, G.N.: 2010, *Astrophys. J.* **719**, L41.
154. Ramesh, R., Kathiravan, C., and Sastry, C.V.: 2010, *Astrophys. J.* **711**, 1029.
155. Reeves, E.M., Foukal, P.V., Huber, M.C.E., Noyes, R.W., Schmahl, E.J., Timothy, J.G., Vernazza, J.E., and Withbroe, G.L.: 1974, *Astrophys. J.* **188**, L27.
156. Raoult, A., Lantos, P., and Fuerst, E.: 1979, *Solar Phys.* **61**, 335.
157. Rempel, M. and Schlichenmaier, R.: 2011, *Living Reviews in Solar Physics* **8**, 3.
158. Rieutord, M. and Rincon, F.: 2010, *Living Reviews in Solar Physics* **7**, 2.
159. Riley, P., Lionello, R., Linker, J.A., Mikic, Z., Luhmann, J., and Wijaya, J.: 2011, *Solar Phys.* **274**, 361.
160. Rutten, R.J., 2003, Radiative Transfer in Stellar Atmospheres, Utrecht University lecture notes, 8th edition.

161. Saito, K., Makita, M., Nishi, K., and Hata, S.: 1970, *Annals of the Tokyo Astronomical Observatory* **12**, 53.
162. Schatzman, E.: 1949, *Annales d'Astrophysique* **12**, 203.
163. Schwarzschild, M.: 1948, *Astrophys. J.* **107**, 1.
164. Schmidt, H.U.: 1964, *NASA Special Publication* **50**, 107.
165. Scudder, J.D.: 1992, *Astrophys. J.* **398**, 319.
166. Selhorst, C.L., Silva, A.V.R., and Costa, J.E.R.: 2004, *Astron. Astroph.* **420**, 1117.
167. Selhorst, C.L., Silva, A.V.R., and Costa, J.E.R.: 2005, *Astron. Astroph.* **433**, 365.
168. Shibasaki, K.: 1999, *Proceedings of the Nobeyama Symposium*, NRO Report 479, 1.
169. Shibasaki, K., Alissandrakis, C.E., and Pohjolainen, S.: 2011, *Solar Phys.* **273**, 309.
170. Shibasaki, K., Enome, S., Nakajima, H., Nishio, M., Takano, T., Hanaoka, Y., Torii, C., Sekiguchi, H., Kawashima, S., Bushimata, T., Shinohara, N., Koshiishi, H., Shiomi, Y., Irimajiri, Y., Leka, K.D., and Canfield, R.C.: 1994, *Publications of the Astronomical Society of Japan* **46**, L17.
171. Silva, A.V.R., Laganá, T.F., Gimenez Castro, C.G., Kaufmann, P., Costa, J.E.R., Levato, H., and Rovira, M.: 2005, *Solar Phys.* **227**, 265.
172. Solanki, S.K., Inhester, B., and Schüssler, M.: 2006, *Reports on Progress in Physics* **69**, 563.
173. Solanki, S.K.: 2003, *Astronomy and Astrophysics Review* **11**, 153.
174. Stenflo, J.O.: 1973, *Solar Phys.* **32**, 41.
175. Sterling, A.C.: 2000, *Solar Phys.* **196**, 79.
176. Stix, M.: 2004, *The sun : an introduction, 2nd ed., Astronomy and astrophysics library, Berlin: Springer, 2004. ISBN: 3540207414*.
177. Strong, K.T., Alissandrakis, C.E., and Kundu, M.R.: 1984, *Astrophys. J.* **277**, 865.
178. Title, A.M. and Schrijver, C.J.: 1998, *Cool Stars, Stellar Systems, and the Sun* **154**, 345.
179. Thejappa, G. and Kundu, M.R.: 1992, *Solar Phys.* **140**, 19.
180. Thejappa, G. and Kundu, M.R.: 1994, *Solar Phys.* **149**, 31.
181. Thejappa, G. and MacDowall, R.J.: 2008, *Astrophys. J.* **676**, 1338.
182. Uralov, A.M., Grechnev, V.V., Rudenko, G.V., Rudenko, I.G., and Nakajima, H.: 2008, *Solar Phys.* **249**, 315.
183. van Ballegooijen, A.A., Asgari-Targhi, M., Cranmer, S.R., and DeLuca, E.E.: 2011, *Astrophys. J.* **736**, 3.
184. van de Hulst, H.C.: 1950, *Bulletin of the Astronomical Institutes of the Netherlands* **11**, 135.
185. Vernazza, J.E., Avrett, E.H., and Loeser, R.: 1973, *Astrophys. J.* **184**, 605.
186. Vernazza, J.E., Avrett, E.H., and Loeser, R.: 1976, *The Astrophysical Journal Supplement Series* **30**, 1.
187. Vernazza, J.E., Avrett, E.H., and Loeser, R.: 1981, *The Astrophysical Journal Supplement Series* **45**, 635.
188. Walsh, R.W. and Ireland, J.: 2003, *Astronomy and Astrophysics Review* **12**, 1.
189. White, S.M., Kundu, M.R., Shimizu, T., Shibasaki, K., and Enome, S.: 1995, *Astrophys. J.* **450**, 435.
190. White, S.M., Loukitcheva, M., and Solanki, S.K.: 2006, *Astron. Astroph.* **456**, 697.
191. Withbroe, G.L. and Noyes, R.W.: 1977, *Annual Review of Astronomy and Astrophysics* **15**, 363.
192. Zaqarashvili, T.V. and Erdélyi, R.: 2009, *Space Science Reviews* **149**, 355.
193. Zhao, J., Kosovichev, A.G., and Sekii, T.: 2010, *Astrophys. J.* **708**, 304.
194. Zhang, J., Kundu, M.R., White, S.M., Dere, K.P., and Newmark, J.S.: 2001, *Astrophys. J.* **561**, 396.
195. Zhang, Y. Z., Shibata, K., Wang, J. X., Mao, X. J., Matsumoto, T., Liu, Y., and Su, J. T.: 2012, *Astrophys. J.*, in press (http://solar.physics.montana.edu/cgi-bin/eprint/index.pl?entry=15970)
196. Zheleznyakov, V.V.: 1962, *Soviet Astronomy* **6**, 3.
197. Zheleznyakov, V.V.: 1970, *Radio emission of the sun and planets*, Oxford: Pergamon Press
198. Zirin, H.: 1988, The Astrophysics of the Sun, *Cambridge University Press*.
199. Zirin, H.: 1966, The Solar Atmosphere, *A Blaisdell Book in the Pure and Applied Sciences, Waltham, Mass.: Blaisdell.*
200. Zirin, H., Baumert, B.M., and Hurford, G.J.: 1991, *Astrophys. J.* **370**, 779.